Atomic-scale imaging of frequency-dependent phonon anisotropy

https://doi.org/10.1038/s41586-025-09511-z

Received: 5 October 2023

Accepted: 11 August 2025

Xingxu Yan[1,7], Paul M. Zeiger[2,7], Yifeng Huang[3,7], Haoying Sun[4], Jie Li[3], Chaitanya A. Gadre[3], Hongbin Yang[1], Ri He[5], Toshihiro Aoki[6], Zhicheng Zhong[5], Yuefeng Nie[4], Ruqian Wu[3]✉, Ján Rusz[2]✉ & Xiaoqing Pan[1,3,6]✉

Directly visualizing vibrational anisotropy in individual phonon modes is essential for understanding a wide range of intriguing optical, thermal and elastic phenomena in materials[1–5]. Although conventional optical and diffraction techniques have been used to estimate vibrational anisotropies, they fall short in achieving the spatial and energy resolution necessary to provide detailed information[4–7]. Here, we introduce a new form of momentum-selective electron energy-loss spectroscopy, which enables the element-resolved imaging of frequency- and symmetry-dependent vibrational anisotropies with atomic resolution. Vibrational anisotropies manifest in different norms of orthogonal atomic displacements, known as thermal ellipsoids. Using the centrosymmetric strontium titanate as a model system, we observed two distinct types of oxygen vibrations with contrasting anisotropies: oblate thermal ellipsoids below 60 meV and prolate ones above 60 meV. In non-centrosymmetric barium titanate, our approach can detect subtle distortions of the oxygen octahedra by observing the unexpected modulation of $\mathbf{q}$-selective signals between apical and equatorial oxygen sites near 55 meV, which originates from reduced crystal symmetry and may also be linked to ferroelectric polarization. These observations are quantitatively supported by theoretical modelling, which demonstrates the reliability of our approach. The measured frequency-dependent vibrational anisotropies shed new light on the dielectric and thermal behaviours governed by acoustic and optical phonons. The ability to visualize phonon eigenvectors at specific crystallographic sites with unprecedented spatial and energy resolution opens new avenues for exploring dielectric, optical, thermal and superconducting properties.

In quantum solid-state theory, the collective vibrations of atoms in a periodic crystal lattice give rise to quasiparticles known as phonons. Recently, there has been growing interest in studying phonon vibrational anisotropy—the variation of phonon spectra along different crystallographic directions—due to its significant impact on the dielectric functions[1], optical responses[2] and thermal properties[3] of low-symmetry materials. For example, anisotropic optical phonon modes within *Reststrahlen* bands generate in-plane polaritons that propagate anisotropically along the surface of two-dimensional (2D) α-MoO_3 films[2,7]. Similarly, due to acoustic phonon anisotropy in layered structures, 2D MoS_2 films with random interlayer rotations exhibit a notable ratio of up to 900 between in-plane and out-of-plane thermal conductivities[3]. Anisotropic atomic vibrations have been found to fundamentally affect the thermal expansion and optical responses of crystals[4–6,8]. Traditionally, angle-resolved polarized Raman spectroscopy has been used to measure phonon anisotropy[7]. However, this approach, along with other phonon-detecting methods such as inelastic neutron scattering, is limited to providing macroscopic measurements with a poor spatial resolution of a few micrometres[9]. Additionally, these methods face drawbacks, such as insufficient energy resolution and the need to average over several phonon modes, resulting in a lack of detailed information about individual phonon branches. By contrast, vibrational anisotropy can occur at the atomic level due to reduced crystal and local point-group symmetries[5]. To directly correlate atomic vibrations with their thermal or optical responses, it is essential to develop experimental techniques capable of observing frequency-resolved eigenvectors at the atomic level.

Recently, monochromated electron energy-loss spectroscopy (EELS) in scanning transmission electron microscopy (STEM) has demonstrated the capability to combine subnanometre spatial resolution with sub-10-meV energy resolution[10]. This method can detect local phonon modes at diverse crystalline imperfections[11–18]. It is also possible to map the intensity fluctuation of vibrational modes near atoms[15,19,20]. However, distinguishing between different elements and resolving

---

[1]Department of Materials Science and Engineering, University of California, Irvine, CA, USA. [2]Department of Physics and Astronomy, Uppsala University, Uppsala, Sweden. [3]Department of Physics and Astronomy, University of California, Irvine, CA, USA. [4]National Laboratory of Solid State Microstructures, Jiangsu Key Laboratory of Artificial Functional Materials, College of Engineering and Applied Sciences, Nanjing University, Nanjing, China. [5]Key Laboratory of Magnetic Materials Devices & Zhejiang Province Key Laboratory of Magnetic Materials and Application Technology, Ningbo Institute of Materials Technology and Engineering, Chinese Academy of Sciences, Ningbo, China. [6]Irvine Materials Research Institute, University of California, Irvine, CA, USA. [7]These authors contributed equally: Xingxu Yan, Paul M. Zeiger, Yifeng Huang. ✉e-mail: wur@uci.edu; jan.rusz@physics.uu.se; xiaoqing.pan@uci.edu

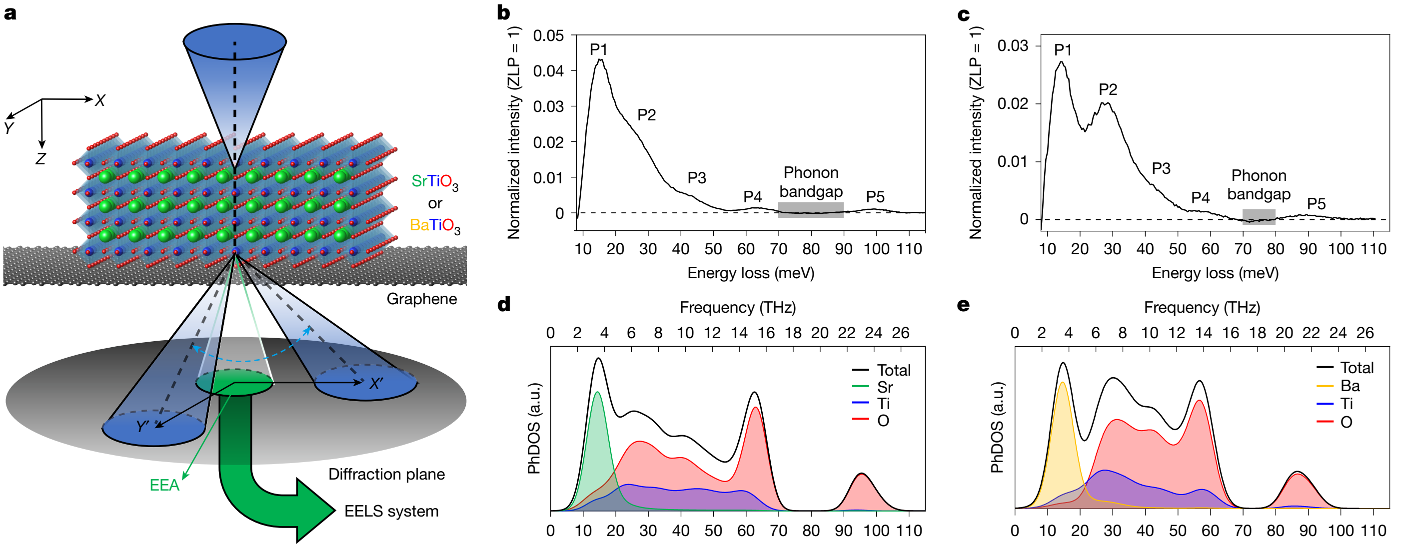

Fig. 1 | Acquisition of vibrational spectra of SrTiO$_3$ and BaTiO$_3$ films. **a**, Schematic of a **q**-selective EELS set-up. An electron beam with a convergence semi-angle of 33 mrad (blue circle) is formed to raster scan on the STO or BTO film with a spatial resolution of 1.5 Å. Transmitted and scattered electrons are deflected by modifying the post-specimen projector lenses to shift the diffraction pattern and move the central disc away from the EELS entrance aperture (EEA) with a collection semi-angle of 25 mrad (green circle) by an angle of 62 mrad to set up **q**-selective EELS conditions. The off-axis electrons are collected to form vibrational spectra in the spectrometer. The STO or BTO film is attached to suspended graphene. Green, blue, red and grey balls denote Sr, Ti, O and C atoms, respectively. **b**, Background-subtracted vibrational spectrum of STO averaged over a 2 nm × 2 nm region. **c**, Background-subtracted vibrational spectrum of BTO averaged over a 2 nm × 2 nm region. **d**, DeePMD-based PhDOS of STO and atom-projected PhDOSs of Sr, Ti and O atoms at 300 K. **e**, DeePMD-based PhDOS of BTO and projected PhDOSs of Ba, Ti and O atoms at 300 K. The phonon bandgap between 70 meV and 90 meV in **d** and that between 70 meV and 80 meV in **e** also appear in the experimental spectra and are used to conduct reliable background subtractions. The PhDOSs in **d** and **e** are broadened with a Gaussian of width 7 meV. Their phonon band structures involve four pairs of longitudinal optical and doubly degenerate transverse optical modes and one pair of longitudinal acoustic and transverse acoustic modes[32,33]. a.u., arbitrary units; ZLP, zero-loss peak.

atomic vibrational anisotropies have yet to be achieved. In this study, we introduce momentum-selective EELS (**q**-selective EELS), which uses a large convergence semi-angle by selectively controlling the momentum exchange of scattered electrons. Unlike angle-resolved phonon measurements that require a small convergence semi-angle, this approach integrates inelastic electron–phonon scattering contributions over several Brillouin zones. As a result, a large convergence semi-angle can be employed to ensure high spatial resolution, without the need for high momentum resolution, according to the intrinsic trade-off between spatial and momentum resolution[13,14]. Our method enables the site-specific detection of vibrational anisotropy for different elements within specific energy ranges. Using centrosymmetric strontium titanate (SrTiO$_3$ or STO) as a model system, we first demonstrate the reliable detection of frequency-dependent anisotropy in oxygen vibrations at various crystallographic sites. Additionally, we reveal that the reduced crystal symmetry and ferroelectric polarization in barium titanate (BaTiO$_3$ or BTO) induce unexpected modulations in vibrational anisotropies for specific phonon modes, which were previously undetectable by other techniques.

Cubic STO is an incipient ferroelectric material with unique dielectric[21,22] and optical properties[23], and it has been extensively used to benchmark new characterization methodologies[24]. The phonon structure of STO is crucial for its antiferrodistortive phase transition at 105 K (ref. 25). By contrast, BTO is in a tetragonal phase with weak spontaneous polarization at room temperature[26]. This lead-free ferroelectric material is widely used in multilayer ceramic capacitors[27] and high-density non-volatile memories[28]. However, the soft-mode-driven displacive ferroelectricity has not been fully explored at the atomic level. Comparative studies of the frequency-dependent vibrational anisotropies of these materials not only test new experimental techniques but also enhance our understanding of the relation between ferroelectricity and certain phonon modes.

Free-standing STO and BTO films were used in the experiments because of their well-controlled composition, uniform thickness and the absence of substrate-induced clamping[29,30]. We transferred 50-unit-cell-thick STO or BTO films (approximately 20 nm) onto a graphene film (3–6 layers) to achieve high-quality hyperspectral imaging datasets. All regions studied are single crystalline and defect-free (Extended Data Fig. 1). The graphene film and residual contamination contribute negligible imaging contrasts and phonon signals in the energy range of interest (Extended Data Fig. 2).

We conducted **q**-selective EELS experiments, as illustrated in Fig. 1a, to measure the localized vibrational signals. Figure 1b shows a background-subtracted vibrational spectrum of STO, revealing five main peaks (P1–P5) at 14.6 meV, 24.4 meV, 41.1 meV, 63.3 meV and 98.7 meV, respectively. To calculate the phonon dispersion curves and phonon density of states (PhDOS) for cubic STO at 300 K, we performed molecular dynamics simulations using a recently developed deep learning potential (DeePMD)[31]. The reliability of the DeePMD method was confirmed by comparing with first-principles calculations (Extended Data Fig. 3) as well as other published experimental and simulation results[32,33] (Extended Data Table 1). The DeePMD-based PhDOS (Fig. 1d) aligns well with the experimental peaks. Accordingly, the P5 peak is attributed to LO4 with predominant oxygen vibrations, P4, P3 and P2 are assigned to TO4/LO3, TO3/LO2 and TO2/LO1 with mixed Ti and O vibrations, respectively, where TO*n* represents transverse optical mode *n* and LO*n* represents longitudinal optical mode *n*. P1 is associated with a combination of TO1, longitudinal acoustic and transverse acoustic modes containing primarily Sr vibrations. Similarly, the background-subtracted vibrational spectrum of BTO in Fig. 1c shows five main peaks at 14.4 meV, 27.7 meV, 41.4 meV, 57.5 meV and 88.8 meV, which are also consistent with the DeePMD-based PhDOS in Fig. 1e. The simulated spectra in Extended Data Fig. 3i–l offer even better consistency with the experimental ones in terms of peak intensity.

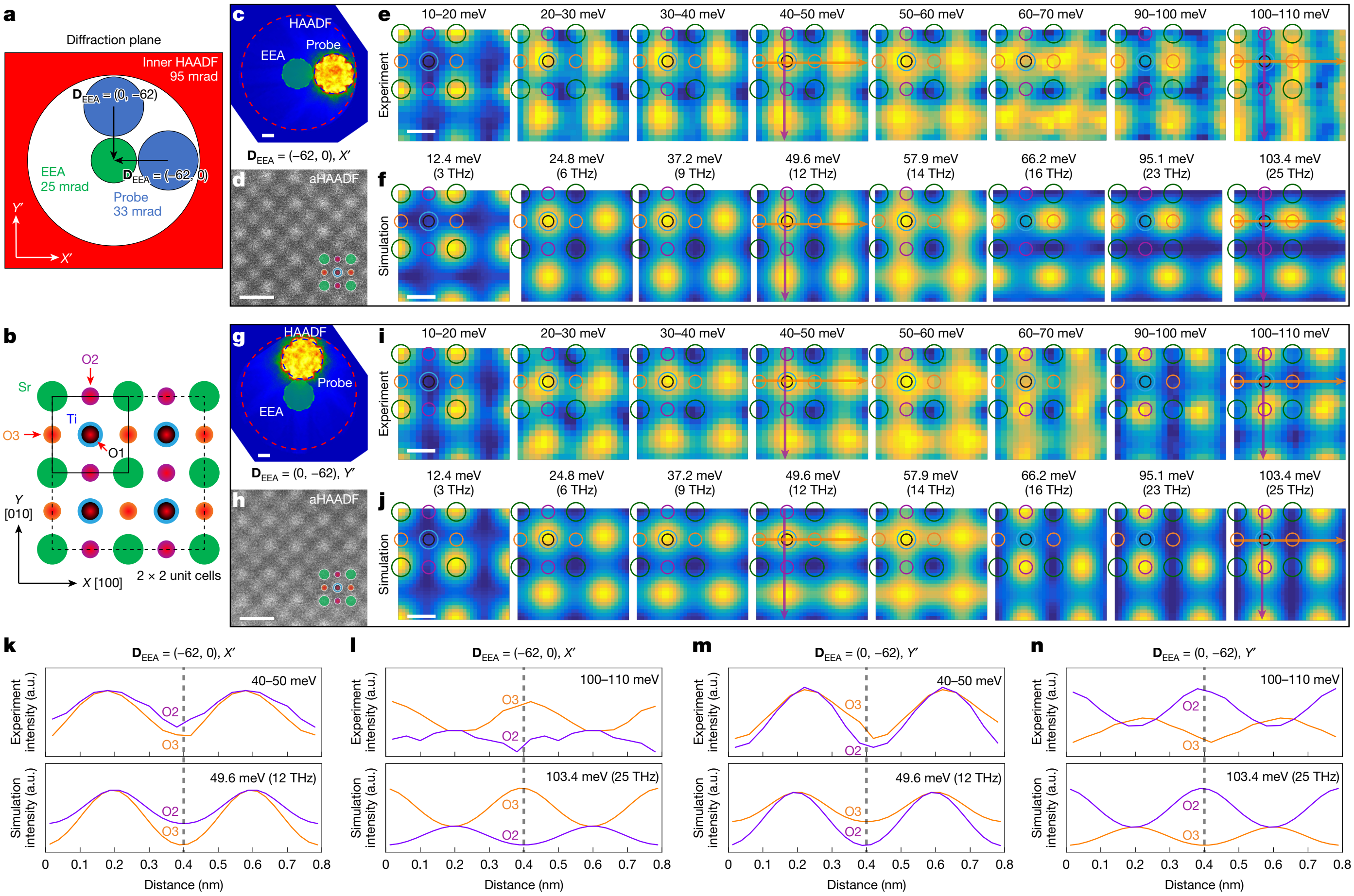

Fig. 2 | Atomic-resolution q-selective EELS signal mapping of STO in different energy ranges with two orthogonal displacement directions of EEA. **a**, Schematic of the diffraction plane showing the movable probe (blue circle), a fixed EEA (green circle) and a HAADF detector (red area). The displacement vector $\mathbf{D}_{\mathrm{EEA}}$ is defined as the vector connecting the centre of the central disc to the centre of the EEA. It quantifies the momentum exchange for scattered electrons. The units of $\mathbf{D}_{\mathrm{EEA}}$ are milliradians, which are omitted in the text. The images were acquired by aHAADF-STEM. **b**, Atomic structure of STO along the [001] direction. The boxes with black solid lines and dashed lines denote a single unit cell and 2 × 2 unit cells, respectively. The oxygen overlapping Ti is labelled as O1 (black), whereas the apical and equatorial oxygen sites are labelled as O2 ($\mathrm{O_{ap}}$, purple) and O3 ($\mathrm{O_{eq}}$, orange), respectively. The [100] and [010] directions are labelled as *X* and *Y* axes in real space and are parallel to the *X′* and *Y′* axes in reciprocal space. **c**–**f**, Representative diffraction pattern (**c**), aHAADF-STEM image (**d**), experimental vibrational signal maps averaged over 25 unit cells in different energy ranges (**e**) and simulated vibrational signal maps (**f**) with $\mathbf{D}_{\mathrm{EEA}} = (-62, 0)$ or an *X′* shift. **g**–**j**, Representative diffraction pattern (**g**), aHAADF-STEM image (**h**), experimental vibrational signal maps averaged over 19 unit cells (**i**) and simulated vibrational signal maps (**j**) with $\mathbf{D}_{\mathrm{EEA}} = (0, -62)$ or a *Y′* shift. Displayed maps are duplicated from single unit cell to 2 × 2 unit cells for visual clarity. Maps for 70–80 meV and 80–90 meV are not given due to the extremely low signals in the phonon bandgap. Simulated maps are blurred with a 2D Gaussian of width 2 Å. The atomic structure of a single unit cell of STO is overlapped on all vibrational signal maps. The green, cyan, black, purple and orange circles denote Sr, Ti, O1, O2 (apical oxygen) and O3 (equatorial oxygen), respectively. **k**–**n**, Comparison of line profiles of vibrational intensities between experiments and simulations in the chosen energy ranges along the horizontal (orange) and vertical (purple) arrows in the corresponding maps: (**k**) 40–50 meV and (**l**) 100–110 meV for an *X′* shift, and (**m**) 40–50 meV and (**n**) 100–110 meV for a *Y′* shift. Scale bars, 20 mrad (**c**,**g**), 5 Å (**d**,**h**), 2 Å (**e**,**f**,**i**,**j**).

Notably, the TO1 mode near 15 meV is identified as the soft-phonon mode responsible for ferroelectricity[25,26]. Compared with previous results[17], A-site Sr or Ba vibration modes below 20 meV are now clearly observed, demonstrating that the state-of-the-art vibrational EELS method effectively resolves phonon modes dominated by heavy elements such as Ba ($Z = 56$). Consequently, the experimental vibrational spectrum captures most phonon modes due to the correction of higher-order EELS aberrations (‘Experimental details’ in Methods).

Based on the atom-projected PhDOS (Fig. 1d,e), we anticipated that the spatial distribution of phonon signals from distinct vibrational states of Sr (Ba), Ti and O would vary across different energy ranges. To test this hypothesis, we conducted atomic-resolution **q**-selective EELS mapping on STO in a controlled manner, as shown in Fig. 2a (‘Experimental details’ in Methods and Extended Data Fig. 4). In the [001] projection, the Sr, Ti/O1, O2 and O3 atomic columns are spatially separated (Fig. 2b). Instead of shifting the diffraction pattern arbitrarily, we moved the central disc along a specific crystallographic direction by a displacement vector $\mathbf{D}_{\mathrm{EEA}}$ to detect phonon eigenmodes along that direction. $\mathbf{D}_{\mathrm{EEA}}$ was chosen as $(-62, 0)$ along *X′* in Fig. 2c or $(0, -62)$ along *Y′* in Fig. 2g ($\mathbf{D}_{\mathrm{EEA}}$ is in units of milliradians). For both shifts, asymmetric high-angle annular dark-field (aHAADF) STEM images (Fig. 2d,h) display the atomic columns of Sr and Ti, indicating a good spatial resolution. The background-subtracted spectra show significant intensity fluctuations (Extended Data Fig. 5a). We applied a series of affine transformations[34] to the energy-filtered vibrational signal maps for individual unit cells to correct for distortions (‘Data analysis and drift correction’ in Methods and Extended Data Fig. 5b,c). The unit-cell-averaged signal maps in Fig. 2e,i (see single unit cells in Extended Data Fig. 6a,b) reveal distinct atomic-resolution features and are in good agreement with simulations using the frequency-resolved frozen phonon multislice (FRFPMS) method[35,36] (Fig. 2f,j and ‘FRFPMS simulations’ in Methods).

Specifically, the 10–20 meV maps show strong intensity at Sr columns. In the medium energy range 20–60 meV, the brightest spots shift to Ti/O1 columns. As the energy loss increases, the surrounding

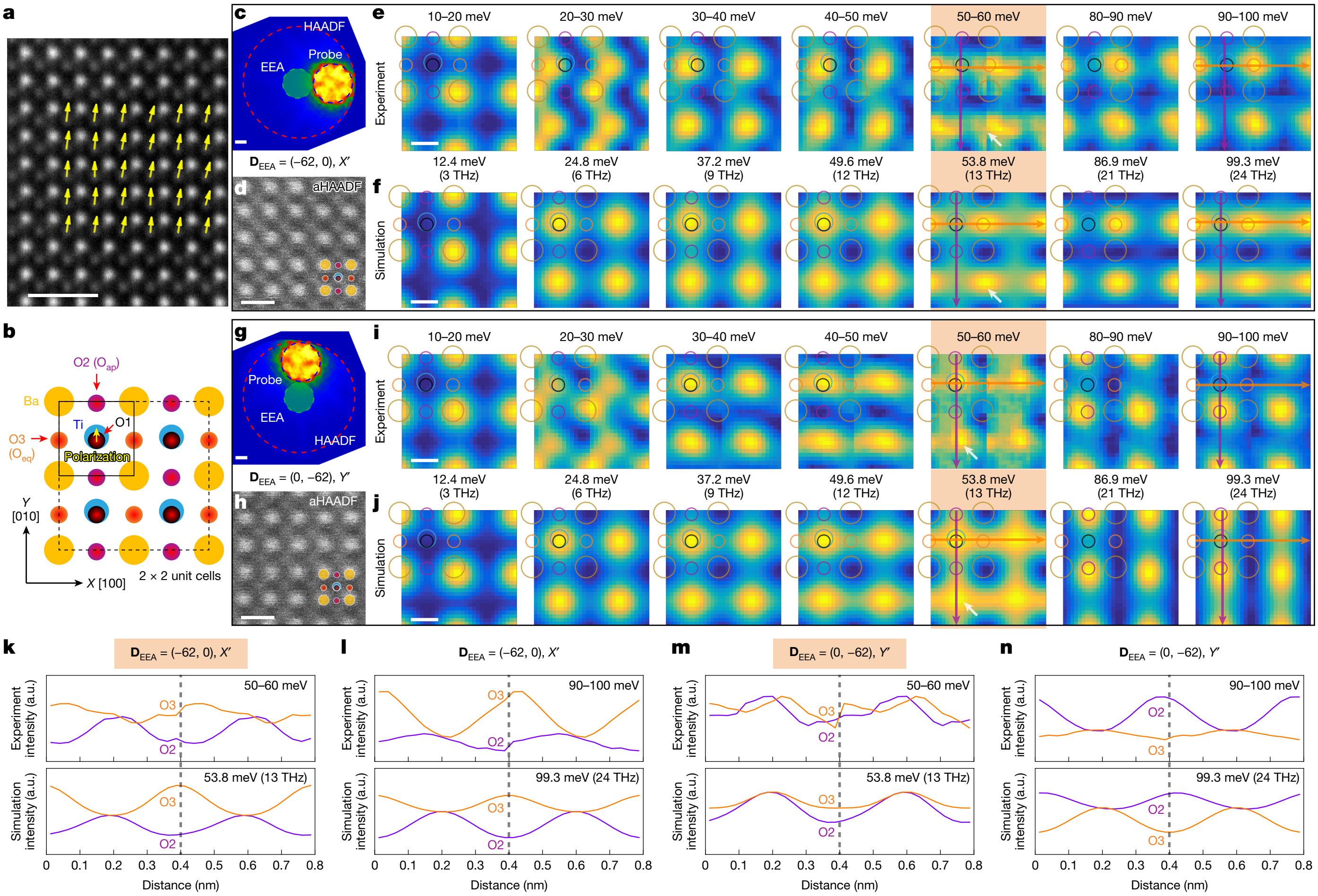

Fig. 3 | Atomic-resolution q-selective EELS signal mapping of BTO. **a**, HAADF-STEM image overlaid with polarization vectors, which are amplified by a factor of 8 for visual clarity. **b**, Atomic structure of BTO along the [010] direction. Gold balls denote Ba atoms. **c**–**f**, Representative diffraction pattern (**c**), aHAADF-STEM image (**d**), experimental vibrational signal maps averaged over 27 unit cells in different energy ranges (**e**) and simulated vibrational signal maps (**f**) with $\mathbf{D}_{EEA}$ = (−62, 0) or an X′ shift. **g**–**j**, Representative diffraction pattern (**g**), aHAADF-STEM image (**h**), experimental vibrational signal maps averaged over 44 unit cells in different energy ranges (**i**) and simulated vibrational signal maps (**j**) with $\mathbf{D}_{EEA}$ = (0, −62) or a Y′ shift. Signal maps for 60–80 meV are not given due to the phonon bandgap. All other details are the same as those in Fig. 2. The orange boxes highlight the energy ranges with large differences in comparison with STO, which are also indicated by white arrows. **k**–**n**, Comparison of line profiles of vibrational intensities between experiments and simulations in chosen energy ranges along the horizontal (orange) and vertical (purple) arrows in the corresponding maps: (**k**) 50–60 meV and (**l**) 90–100 meV for an X′ shift, and (**m**) 50–60 meV and (**n**) 90–100 meV for a Y′ shift. Scale bars, 1 nm (**a**), 20 mrad (**c**,**g**), 5 Å (**d**,**h**), 2 Å (**e**,**f**,**i**,**j**).

oxygen columns become progressively brighter, a trend more pronounced in the raw simulation results (Extended Data Fig. 6e,f). By contrast, in higher energy ranges (60–70 meV and 90–110 meV), the O2 and O3 columns show the strongest intensities, whereas the Ti/O1 and Sr columns seem dimmer. Although oxygen atoms are not visible in aHAADF-STEM images (Fig. 2d,h), the vibrational signal maps reveal their positions.

We performed similar experiments on a region of BTO with ferroelectric polarizations along [001] (Fig. 3a,b). Figure 3c–j displays the energy-filtered vibrational signal maps. As the energy loss increases, the bright spots in each map shift from Ba to Ti/O1 and then to pure oxygen columns, consistent with the simulation results. One main discrepancy is that both Ba and Ti/O1 are visible in the experimental maps of 20–30 meV, whereas only Ti/O1 appears in the simulation results. This may arise from the non-zero Ba-projected PhDOS in that energy range and spectral broadening effects (‘Possible sources of map differences’ in Methods). We also carried out multi-frame EELS experiments over larger regions, finding consistent atomic features (Extended Data Fig. 7). Our method obtained element-resolved mapping of both heavy and light elements. These results clearly demonstrate that phonon wavefunctions (or eigenvectors) exhibit atomic-level fluctuations and vary across different atomic columns. This provides more concrete evidence than previously reported for atomic-level signal fluctuations[19,20], which can be attributed to electrons undergoing increased inelastic scattering and yielding stronger phonon signals at atomic columns compared with the positions between them.

Notably, intriguing differences arise between X′- and Y′-shifted results. For instance, in the 40–50 meV map of STO for the X′ shift, the O2 columns exhibit stronger intensities than the O3 columns, whereas for the Y′ shift, O3 is more intense than O2. This directional dependence is even more pronounced in the 100–110 meV maps, where only O3 (O2) atoms are prominent for the X′ (Y′) shift. These variations can be understood by recognizing that high-energy LO4 phonons manifest as breathing modes of the oxygen octahedra[37]. The intensity variations of the corresponding line profiles quantitatively match the simulated results in Fig. 2k–n. From a symmetry perspective, STO has a centrosymmetric cubic structure (*Pm*-3*m*) at room temperature, so one would not expect any macroscopic anisotropic properties[5]. However, only Sr and Ti sites adhere to the full point-group symmetry (O_h), whereas oxygen atoms have lower site symmetry (D_{4h}). Specifically, along [001], O1 has fourfold rotational symmetry (C_4), whereas O2 and O3 are invariant under twofold rotations and mirroring. The reduced point-group

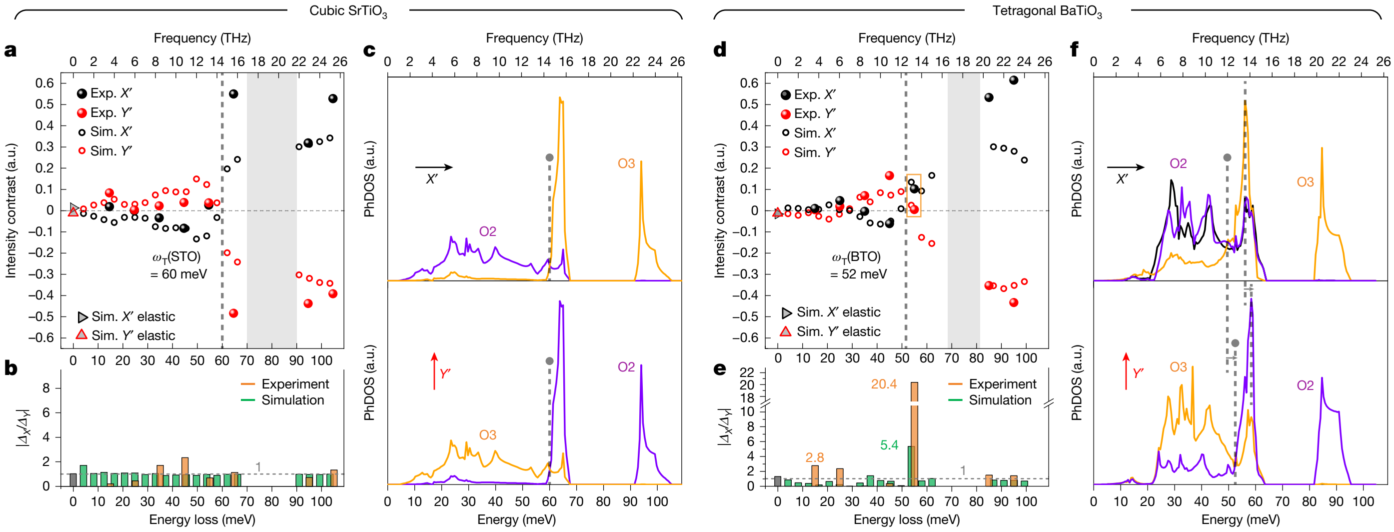

Fig. 4 | Quantitative analysis of vibrational anisotropies of oxygen atoms in STO and BTO in different energy ranges. **a**, Intensity contrast between O3 and O2 columns from experimental and simulated energy-filtered vibrational signal maps of STO for both an *X′* shift (Δ_X) and a *Y′* shift (Δ_Y). $\Delta_i = (I_{O3} - I_{O2})/(I_{O3} + I_{O2})$, where I_{O3} and I_{O2} represent the signal intensities at the O3 and O2 positions, respectively. **b**, Ratio of intensity contrast $|\Delta_X/\Delta_Y|$ for STO. Most ratios span from 0.5 to 1.7, with two outliers of 0.2 in the 10–20 meV range and 2.3 in the 30–40 meV range. **c**, Projected PhDOSs of O1 (black), O2 (purple) and O3 (orange) atoms in STO along the *X′* (top) and *Y′* (bottom) directions. The O1 curve overlaps the O2 (O3) one in the top (bottom) panel. The measured transition energy ω_T of STO (60 meV) is in good agreement with the crossover points where the magnitudes of the projected PhDOS for O2 and O3 are equal. **d**, Intensity contrast between O3 and O2 columns from experimental and simulation results for BTO. The orange box indicates the asymmetric intensity contrasts in 50–60 meV. **e**, Ratio of intensity contrast $|\Delta_X/\Delta_Y|$ for BTO. Most ratios fluctuate in a wider range of 0.4–2.8 with one outlier of 0.0431 in the 30–40 meV range. **f**, Projected PhDOSs of three oxygen atoms in BTO. The crossover points are 49.6 meV for the *X′* component and 52.8 meV for the *Y′* component. The positions of O3 and O2 columns are labelled as orange and purple circles, respectively, in Figs. 2 and 3. The grey areas in **a** and **d** indicate the phonon bandgaps. The triangles at 0 meV in **a** and **d** are the calculated intensity contrasts between O3 and O2 from elastic scattering signals in Extended Data Fig. 8, which are extremely small ($|\Delta_i| < 0.02$) for both STO and BTO. The vertical dashed lines denote the position of transition energies and crossover points. The energy position of the highest $|\Delta_X/\Delta_Y|$ for BTO is approximately 55 meV (13 THz) and is close to the transition energy ω_T of BTO (52 meV). Exp. experiment; Sim., simulation; a.u., arbitrary units.

symmetry at O2 or O3 influences inelastically scattered electrons but not elastically scattered ones at higher scattering angles (Extended Data Fig. 8). The asymmetric distributions of inelastically scattered electrons result in noticeable variations in **q**-selective EELS signals between orthogonal directions. A similar directional dependence is observed in BTO. In the 90–100 meV range, the *X′* shift results in brighter O3 (O_{eq}), whereas the *Y′* shift produces brighter O2 (O_{ap}), as shown in both maps and line profiles of Fig. 3k–n. Therefore, vibrational signals associated with different oxygen sites show altered intensities depending on the momentum exchange and energy range.

The directional dependence in BTO is more complex due to the lower point-group symmetries for apical (C_{4v}) and equatorial (C_{2v}) oxygen atoms and the lack of fourfold rotational symmetry between [001] and [100]/[010], as depicted in Fig. 3b. To better understand the variations, we introduce an intensity contrast, Δ_i ($i = X$ or Y) to quantify the signal difference between O3 and O2. Figure 4a reveals anisotropies ($\Delta_i \neq 0$) in almost all energy ranges for STO. Specifically, Δ_X is negative below a transition energy (ω_T) of 60 meV, then it becomes positive at higher energies. Δ_Y shows a symmetric reversal. Measured Δ_i values match the simulations, indicating that our method could potentially derive the amplitude of individual atomic vibrations. The same analysis for BTO unveils comparable trends (Fig. 4d). Note that the elastic scattering signals give rise to negligible intensity contrasts. However, several differences between STO and BTO are evident. First, Δ_X of BTO is positive below 30 meV, becomes negative from 30 meV to 52 meV, and turns positive again above 52 meV. Second, ω_T of BTO decreases to around 52 meV due to its distinct composition and structure. Third, the absolute values of Δ_i are no longer identical between orthogonal directions in BTO. To further visualize asymmetric modulations, we computed $|\Delta_X/\Delta_Y|$ (Fig. 4b,e). $|\Delta_X/\Delta_Y|$ in STO theoretically equals 1, and most measured values are reasonably close to 1. By contrast, $|\Delta_X/\Delta_Y|$ in BTO can reach extremely high values (20.4 in 50–60 meV and 2.8 in 10–20 meV).

Such intensity variations can be explained by considering the scattering probability of fast electrons interacting with lattice vibrations and the PhDOS[15]. Its selection rule is rooted in the term $\mathbf{q} \cdot \mathbf{e}_i(\omega)$, where $\mathbf{q}$ is the momentum exchange and $\mathbf{e}_i(\omega)$ is the phonon eigenvector of atom *i* at frequency *ω*. As vibrational EELS is primarily sensitive to vibrations perpendicular to the beam direction[9], we focus on the *X′* and *Y′* components of oxygen-projected PhDOS in Fig. 4c,f. For the *X′* component in STO, O1 and O2 have similar PhDOSs, whereas O3 shows a distinct curve. Below 60 meV (ω_T), the PhDOS of O2 is higher than that of O3, whereas above 60 meV, the PhDOS of O3 increases and even dominates in 90–110 meV. Conversely, the *Y′* components show the reverse trend. Therefore, the oxygen-projected PhDOSs are consistent with our experimental observations, indicating that modulations result from the anisotropy of phonon eigenvectors.

The large $|\Delta_X/\Delta_Y|$ in BTO can be interpreted by examining peak shifts in the oxygen-projected PhDOS (Fig. 4f). The cation displacement and oxygen-octahedra distortion in tetragonal BTO lead to a shorter distance from Ti to O_{ap} compared with Ti–O_{eq}. This results in a stronger Ti–O_{ap} bond with a larger force constant. Consequently, Ti–O vibrations along *Y′* have higher energies than those along *X′*, as evidenced by a blueshift of 2.3 meV between the highest PhDOS peak and a blueshift of 3.2 meV between crossover points. Such energy discrepancies result in altered vibrational signals in 50–60 meV, with O_{eq} and O_{ap} exhibiting similar intensities for the *Y′* shift and O_{eq} showing stronger signals for the *X′* shift. Simulations confirm that $|\Delta_X/\Delta_Y|$ deviates from 1, with a notable high value of 5.4 at approximately 55 meV.

The observed frequency- and symmetry-dependent modulations at different crystallographic sites reflect the three-dimensional vibrational behaviour of individual atoms around their equilibrium positions. To better visualize anisotropies, we plot the diagonal elements of the frequency-dependent anisotropic displacement parameters (ADPs), commonly known as thermal ellipsoids, in Extended Data Fig. 9.

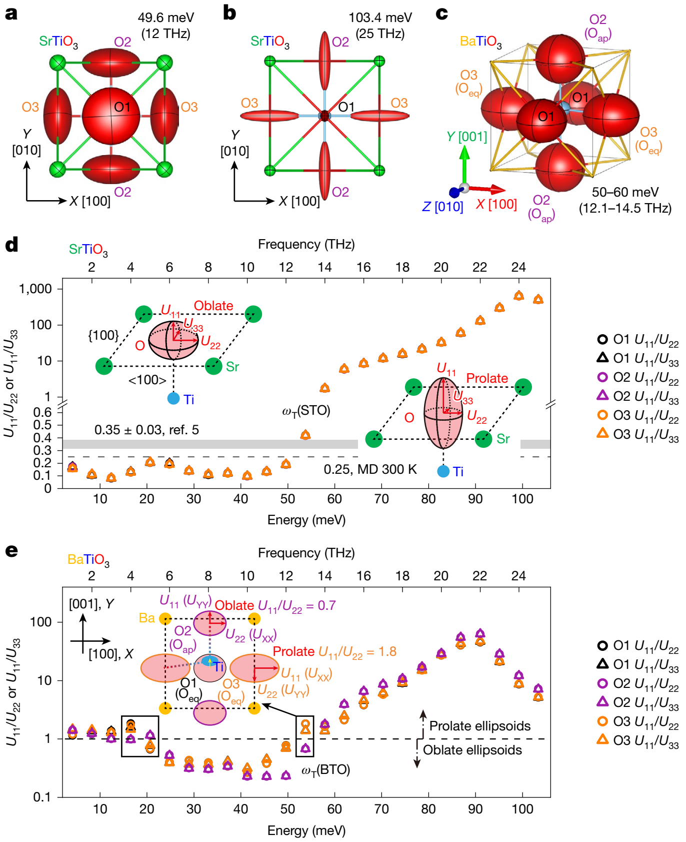

Fig. 5 | Simulated frequency-dependent thermal ellipsoids of oxygen atoms in STO and BTO. a,**b**, [001]-projected thermal ellipsoids representing the anisotropy of all atoms in STO around 49.6 meV (12 THz, **a**) and 103.4 meV (25 THz, **b**), respectively. **c**, Oblique view of thermal ellipsoids of all atoms of BTO in the range 50–60 meV (12.1–14.5 THz). The size of ADPs in **a**–**c** is exaggerated for visual clarity (Extended Data Fig. 9). **d**, Aspect ratio (U_{11}/U_{22} or U_{11}/U_{33}) of thermal ellipsoids of oxygen atoms in STO versus energy. The dashed line and grey band represent the aspect ratios of the total oxygen thermal ellipsoids calculated from our molecular dynamics calculations at 300 K and from ref. 5, respectively. Insets, Schematic illustration showing that U_{11} is a one-dimensional vibration along the O–Ti direction. U_{22} and U_{33} correspond to a 2D vibration ($U_{22} = U_{33}$) in the O–Sr plane for the oblate and prolate ellipsoids of all oxygen sites. **e**, Aspect ratio of thermal ellipsoids of oxygen atoms in BTO versus energy. The black boxes indicate the frequencies where the prolate and oblate ellipsoids coexist. Inset, schematic illustration showing that apical oxygen atoms (O2) and equatorial oxygen atoms (O1 and O3 in the equatorial plane of TiO_6 octahedra) exhibit dissimilar thermal ellipsoids at 53.8 meV (13 THz), in which the ADP along the *X* direction (U_{XX}) is U_{22} for O2 and U_{11} for O3 and U_{YY} is U_{11} for O2 and U_{22} for O3 to better describe their directional dependence. Besides 53.8 meV, oblate and prolate ellipsoids also coexist at 16.5 meV and 20.7 meV (Extended Data Fig. 9b). MD, molecular dynamics.

The simulated thermal ellipsoids of oxygen atoms in STO exhibit a notable change in shape with energy: they transition from oblate ellipsoids below ω_T(STO) to prolate ellipsoids above ω_T(STO), as illustrated in Fig. 5a,b. There is a 90° rotational symmetry between the thermal ellipsoids of O2 and O3, resulting in different vibrational signals acquired under different momentum exchanges. Quantitatively, we assess the ellipticities and anisotropies using the aspect ratio of ADPs along the O–Ti direction (U_{11}) and those in the O–Sr plane (U_{22} or U_{33}). In STO (Fig. 5d), all oxygen atoms display similar aspect ratios, fluctuating between 0.08 and 0.20 below 50 meV, which are lower than the overall ones[4–6,8]. These reduced aspect ratios indicate significant anisotropies for acoustic and soft-phonon modes, which are crucial for heat transport. The precise measurement of these anisotropies represents a substantial advance over traditional diffraction methods. Large oxygen vibrations in the O–Sr planes are associated with the libration of TiO_6 octahedra, a precursor to the antiferrodistortive phase transition of STO[6,8]. Future studies, potentially using cryogenic stages[38], could explore the energy shifts of soft-phonon modes to understand the origins of ferroelectricity at lower temperatures[25]. In higher energy ranges, the aspect ratios are larger than 1, reaching a maximum of approximately 630 at 99.3 meV, indicating greatly enhanced anisotropies for optical phonon modes. For LO4 phonons, the oxygen atoms vibrate almost exclusively along the O–Ti bonding direction and can be coupled with mid-infrared optical lasers to induce a photoflexoelectric response[23].

The simulated ADPs for BTO offer deeper insights into the unexpected modulations. Figure 5e presents identical ratios for O1 and O3 but distinct ratios for O2. These deviations are evident in three energy ranges: 12–16 meV, 45–53 meV and over 87 meV, which help explain the huge ratio of intensity contrasts observed near ω_T(BTO). At 53.8 meV, ADPs along *Y* of O2 ($U_{11} = 1.52 \times 10^{-4}$ Å^2) and O3 ($U_{22} = 1.64 \times 10^{-4}$ Å^2) are close to each other, but the ADP along *X* of O2 ($U_{22} = 2.23 \times 10^{-4}$ Å^2) is smaller than that of O3 ($U_{11} = 2.99 \times 10^{-4}$ Å^2). This disparity leads to the concurrence of oblate and prolate ellipsoids in 50–60 meV (Fig. 5c). The polarization-induced shortening of Ti–O_{ap} bonds probably drives the non-degenerate thermal ellipsoids of O_{ap} and O_{eq}. Additionally, the higher ratio of $|\Delta_X/\Delta_Y|$ in 10–20 meV may be linked to soft phonons and the associated ferroelectric polarization and oxygen-octahedra distortion.

In conclusion, our **q**-selective EELS method is a powerful tool for element-resolved and atomic site-specific analyses of phonon eigenvectors in complex perovskite oxides. We have demonstrated that oxygen atoms in STO and BTO exhibit distinct anisotropic vibrations along orthogonal directions at medium and high phonon energies. The asymmetric modulations between apical and equatorial oxygen atoms in BTO arise from its reduced crystal symmetry and might be indicative of spontaneous polarization and oxygen-octahedra distortion in ferroelectric materials. We also note that multislice electron ptychography has successfully detected thermal vibrations at atomic resolution[39], but it still lacks the energy resolution needed to distinguish the thermal ellipsoids of different phonon modes. The ability to map vibrational anisotropy with unprecedented spatial and energy resolution opens avenues for further studies on ferroelectric phase transitions, the origins of ferroelectricity and the role of apical oxygen sites in modifying exchange interactions in high-temperature superconductors[40,41]. Furthermore, exploring **q**-selective EELS signals with certain momentum exchanges could enable precise measurements of polarization vectors and associated oxygen-octahedra distortion for displacive ferroelectrics. For instance, selecting the ⟨111⟩ direction may facilitate the study of spontaneous polarization in $BiFeO_3$ in a pseudo-cubic phase[42].

Online content

Any methods, additional references, Nature Portfolio reporting summaries, source data, extended data, supplementary information, acknowledgements, peer review information; details of author contributions and competing interests; and statements of data and code availability are available at https://doi.org/10.1038/s41586-025-09511-z.

1. Schubert, M. et al. Anisotropy, phonon modes, and free charge carrier parameters in monoclinic β-gallium oxide single crystals. *Phys. Rev. B* **93**, 125209 (2016).
2. Ma, W. L. et al. In-plane anisotropic and ultra-low-loss polaritons in a natural van der Waals crystal. *Nature* **562**, 557–562 (2018).
3. Kim, S. E. et al. Extremely anisotropic van der Waals thermal conductors. *Nature* **597**, 660–665 (2021).
4. Bubnova, R., Volkov, S., Albert, B. & Filatov, S. Borates—crystal structures of prospective nonlinear optical materials: high anisotropy of the thermal expansion caused by anharmonic atomic vibrations. *Crystals* **7**, 93 (2017).
5. Lin, I. C. et al. Extraction of anisotropic thermal vibration factors for oxygen from the Ti $L_{2,3}$-edge in $SrTiO_3$. *J. Phys. Chem. C* **127**, 17802–17808 (2023).

6. Abramov, Y. A., Tsirelson, V. G., Zavodnik, V. E., Ivanov, S. A. & Brown, I. D. The chemical bond and atomic displacements in $SrTiO_3$ from X-ray diffraction analysis. *Acta Crystallogr. B* **51**, 942–951 (1995).
7. Gong, Y. et al. Polarized Raman scattering of in-plane anisotropic phonon modes in α-MoO_3. *Adv. Opt. Mater.* **10**, 2200038 (2022).
8. Jauch, W. & Reehuis, M. Electron-density distribution in cubic $SrTiO_3$: a comparative gamma-ray diffraction study. *Acta Crystallogr. A* **61**, 411–417 (2005).
9. Yan, X., Gadre, C. A., Aoki, T. & Pan, X. Probing molecular vibrations by monochromated electron microscopy. *Trends Chem.* **4**, 76–90 (2022).
10. Krivanek, O. L. et al. Vibrational spectroscopy in the electron microscope. *Nature* **514**, 209–212 (2014).
11. Hage, F. S., Radtke, G., Kepaptsoglou, D. M., Lazzeri, M. & Ramasse, Q. M. Single-atom vibrational spectroscopy in the scanning transmission electron microscope. *Science* **367**, 1124–1127 (2020).
12. Xu, M. et al. Single-atom vibrational spectroscopy with chemical-bonding sensitivity. *Nat. Mater.* **22**, 612–618 (2023).
13. Yan, X. et al. Single-defect phonons imaged by electron microscopy. *Nature* **589**, 65–69 (2021).
14. Qi, R. et al. Measuring phonon dispersion at an interface. *Nature* **599**, 399–403 (2021).
15. Gadre, C. A. et al. Nanoscale imaging of phonon dynamics by electron microscopy. *Nature* **606**, 292–297 (2022).
16. Zeiger, P. M. & Rusz, J. Simulations of spatially and angle-resolved vibrational electron energy loss spectroscopy for a system with a planar defect. *Phys. Rev. B* **104**, 094103 (2021).
17. Hoglund, E. R. et al. Direct visualization of localized vibrations at complex grain boundaries. *Adv. Mater.* **35**, e2208920 (2023).
18. Haas, B. et al. Atomic-resolution mapping of localized phonon modes at grain boundaries. *Nano Lett.* **23**, 5975–5980 (2023).
19. Hage, F. S., Kepaptsoglou, D. M., Ramasse, Q. M. & Allen, L. J. Phonon spectroscopy at atomic resolution. *Phys. Rev. Lett.* **122**, 016103 (2019).
20. Venkatraman, K., Levin, B. D. A., March, K., Rez, P. & Crozier, P. A. Vibrational spectroscopy at atomic resolution with electron impact scattering. *Nat. Phys.* **15**, 1237–1241 (2019).
21. Sirenko, A. A. et al. Soft-mode hardening in $SrTiO_3$ thin films. *Nature* **404**, 373–376 (2000).
22. Huang, J. K. et al. High-kappa perovskite membranes as insulators for two-dimensional transistors. *Nature* **605**, 262–267 (2022).
23. Nova, T. F., Disa, A. S., Fechner, M. & Cavalleri, A. Metastable ferroelectricity in optically strained $SrTiO_3$. *Science* **364**, 1075–1079 (2019).
24. Gao, W. et al. Real-space charge-density imaging with sub-ångström resolution by four-dimensional electron microscopy. *Nature* **575**, 480–484 (2019).
25. Casella, L. & Zaccone, A. Soft mode theory of ferroelectric phase transitions in the low-temperature phase. *J. Phys. Condens. Matter* **33**, 165401 (2021).
26. Burns, G. & Dacol, F. H. Lattice modes in ferroelectric perovskites. III. Soft modes in $BaTiO_3$. *Phys. Rev. B* **18**, 5750–5755 (1978).
27. Tian, Z. et al. Preparation of nano $BaTiO_3$-based ceramics for multilayer ceramic capacitor application by chemical coating method. *J. Am. Ceram. Soc.* **92**, 830–833 (2009).
28. Jeong, D. S. et al. Emerging memories: resistive switching mechanisms and current status. *Rep. Prog. Phys.* **75**, 076502 (2012).
29. Ji, D. et al. Freestanding crystalline oxide perovskites down to the monolayer limit. *Nature* **570**, 87–90 (2019).
30. Sun, H. et al. Nonvolatile ferroelectric domain wall memory integrated on silicon. *Nat. Commun.* **13**, 4332 (2022).
31. He, R. et al. Structural phase transitions in $SrTiO_3$ from deep potential molecular dynamics. *Phys. Rev. B* **105**, 064104 (2022).
32. van der Marel, D., Barantani, F. & Rischau, C. W. Possible mechanism for superconductivity in doped $SrTiO_3$. *Phys. Rev. Res.* **1**, 013003 (2019).
33. Niedermeier, C. A. et al. Phonon scattering limited mobility in the representative cubic perovskite semiconductors $SrGeO_3$, $BaSnO_3$, and $SrTiO_3$. *Phys. Rev. B* **101**, 125206 (2020).
34. Smith, J., Huang, Z., Gao, W., Zhang, G. & Chi, M. Atomic resolution cryogenic 4D-STEM imaging via robust distortion correction. *ACS Nano* **17**, 11327–11334 (2023).
35. Zeiger, P. M. & Rusz, J. Efficient and versatile model for vibrational STEM-EELS. *Phys. Rev. Lett.* **124**, 025501 (2020).
36. Zeiger, P. M. & Rusz, J. Frequency-resolved frozen phonon multislice method and its application to vibrational electron energy loss spectroscopy using parallel illumination. *Phys. Rev. B* **104**, 104301 (2021).
37. Cancellieri, C. et al. Polaronic metal state at the $LaAlO_3/SrTiO_3$ interface. *Nat. Commun.* **7**, 10386 (2016).
38. Krivanek, O. et al. Damage-free analysis of biological materials by vibrational spectroscopy in the EM. *Microsc. Microanal.* **26**, 108–110 (2020).
39. Chen, Z. et al. Electron ptychography achieves atomic-resolution limits set by lattice vibrations. *Science* **372**, 826–831 (2021).
40. Sun, H. et al. Signatures of superconductivity near 80 K in a nickelate under high pressure. *Nature* **621**, 493–498 (2023).
41. Yang, H. et al. Phonon modes and electron–phonon coupling at the $FeSe/SrTiO_3$ interface. *Nature* **635**, 332–336 (2024).
42. Nelson, C. T. et al. Domain dynamics during ferroelectric switching. *Science* **334**, 968–971 (2011).

Publisher's note Springer Nature remains neutral with regard to jurisdictional claims in published maps and institutional affiliations.

Methods

Sample preparation

A water-soluble $Sr_3Al_2O_6$ (SAO) film was first grown on a (001) TiO_2-terminated STO single-crystalline substrate followed by the growth of a thin STO film by oxide molecular beam epitaxy. During the growth, reflection high-energy electron diffraction was used to monitor the surface quality and allow us to precisely control the thickness of the films according to the intensity oscillations. A 6-unit-cell-thick SAO layer was first deposited at a substrate temperature of 850 °C with an oxygen pressure of 1×10^{-6} Torr. For STO films, a 50-unit-cell-thick STO layer was subsequently deposited at a relatively lower temperature of 650 °C to reduce the diffusion of Ti atoms into SAO layers. For BTO films, a 50-unit-cell-thick BTO layer was subsequently deposited at 850 °C with an oxygen pressure of 1×10^{-6} Torr (10% ozone and 90% oxygen). To prepare the transmission electron microscopy (TEM) specimens, the STO/SAO/STO or BTO/SAO/STO film was immersed into deionized water at room temperature until the sacrificial SAO layer was completely dissolved, and the peeled STO or BTO film was floating on the water surface. Then, the free-standing film was picked up by lacey carbon TEM grids covered with a few-layer graphene film (Ted Pella) under an optical microscope. Each STO/graphene and BTO/graphene TEM specimen was baked for over 24 h at 160 °C before inserting into the microscope.

Experimental details

Low-magnification TEM images and selected area diffraction patterns were obtained using a JEOL 2100 F TEM operating at 200 kV. Low-magnification HAADF-STEM imaging and elemental mapping using energy-dispersive X-ray spectrometry were performed on a JEOL JEM-ARM300F S/TEM, equipped with double correctors and dual large-angle energy-dispersive X-ray spectrometers, with a convergence semi-angle of 22 mrad and inner and outer collection angles of 83 mrad and 165 mrad. STEM images, core-loss EELS and **q**-selective EELS spectra were collected by a Nion UltraSTEM 200 equipped with C3/C5 aberration corrector and high-energy-resolution monochromated EELS system (HERMES). The convergence semi-angle of the 60 kV electron probe was 33 mrad with a beam current of approximately 100 pA before monochromation. The inner and outer collection semi-angles of the HAADF detector were 95 mrad and 210 mrad, respectively. The dwell time of HAADF images without monochromation was 8 µs, whereas that with monochromation was 20 µs. The collection semi-angle of EEA was 25 mrad. The microscope condition was carefully tuned to centre the electron probe, HAADF detector and EEA with a Ronchigram camera before changing to off-axis EELS settings. The *X* and *Y* directions of the STO or BTO films studied were identified from atomic-resolution STEM images and used to set up the displacement direction of the diffraction pattern on the Ronchigram camera using post-specimen projector lenses. To accurately correlate the directions in the diffraction plane with crystalline orientations, we measured the rotation angle (178.5° in our experimental condition) between the sample plane and the diffraction plane by comparing the same feature (for example, sample edges) in both over-focused and under-focused shadow images with that in a low-magnification STEM image[43]. This rotation angle was considered when shifting the diffraction patterns along either the *X′* or *Y′* direction of STO and BTO. The displacement distance of EEA ($\mathbf{D}_{EEA}$) was set to 62 mrad to avoid any overlap between the central disc and EEA or between the central disc and the HAADF detector to satisfy the rigorous dark-field imaging and spectroscopic conditions and to optimize the recorded phonon signals. An alpha-type monochromator was activated to obtain the best energy resolution of 5.7 meV under the regular on-axis condition. Monochromator slit aberrations, monochromator exit aberrations, probe aberrations, projector aberrations and EELS aberrations were all corrected to guarantee sufficient spatial resolution and the best and stable energy resolution after monochromation. Most importantly, to routinely achieve a good energy resolution (9–15 meV), which was measured as the full-width at half-maximum of the ZLP, under the **q**-selective EELS condition, the magnitudes of second-order EELS aberrations were tuned to be less than 100 V and the magnitudes of the third-order EELS aberrations were tuned to be less than 1,000 V. The EELS dispersion was set to about 0.5 meV per channel and calibrated frequently by wobbling the drift tube. The polarization vectors of the BTO films studied were obtained from atomic-resolution STEM images captured under the high spatial resolution of a 38-mrad convergence semi-angle and a 10-pA beam current with a multi-frame acquisition of aligning and summing 40 frames with a short dwell time of 2 µs pix^{-1} to improve the measurement precision. The off-centre shifts of Ti atoms were measured by identifying the position of both Ba and Ti atoms in the STEM images by employing a 2D Gaussian fitting algorithm in the Atomap package[44].

Atomic-resolution hyperspectral images of vibrational signals were acquired by running the built-in Spectrum Imaging function in Nion's Swift software. The field of view of the mapping area was 1.5–2.0 nm and contained four or five unit cells of STO or BTO with 45–60 pix in each direction. Each spectrum was acquired as a single frame with 1 s of exposure time per pixel. The total acquisition time of hyperspectral image dataset was 30–60 min to ensure a decent probe current without significant decay and to reduce the impact of sample drift. The datasets used for extracting the atomic-resolution hyperspectral images must have a sample drift less than 0.8 nm (approximately two unit cells) without a noticeable focus change or contamination, which was examined by comparing the STEM images before and after vibrational EELS acquisition. One example is shown in Extended Data Fig. 4.

To acquire hyperspectral images of vibrational signals over larger regions of STO and BTO, a multi-frame EELS acquisition method was applied with an exposure time of 100 ms per pixel, 45 × 45 pixels (3 nm × 3 nm) and approximately 60 frames in total for each **q**-selective EELS condition. Then, the multi-frame hyperspectral images were aligned using a rigid image registration algorithm based on simultaneous aHAADF-STEM images to achieve the cropped regions of approximately 2.3 nm × 2.3 nm, and the vibrational spectra were aligned on the ZLP peak centre. The pixel size in the multi-frame EELS datasets on the larger region was about 0.066 nm pix^{-1}, which is larger than that used (0.033 nm pix^{-1}) for single-unit-cell maps. Thus, the single-unit-cell energy-filtered vibrational signal maps in Figs. 2 and 3 offer finer spatial details.

Data analysis and drift correction

Hyperspectral image datasets were aligned by the ZLP centre and normalized by the ZLP height. To improve the signal-to-noise ratio and make the data analysis more reliable, all hyperspectral image datasets were binned for each 4 × 4 pixel area. Then, background subtraction was carefully conducted by setting three fitting windows and fitting a power law function as $I(E) = aE^{-b} + c$, where $I(E)$ is the intensity of vibrational spectrum, E is the energy loss in units of milli-electronvolts and a, b and c are fitting coefficients[45]. The fitting windows were selected based on the materials and the phonon energies of interest. The fitting windows for most STO results were 7–9 meV, 75–85 meV and 110–130 meV to match the energy span of the main peaks in the calculated PhDOS and energy bandgap (70–90 meV), whereas those for most BTO results were 8–9 meV, 72–80 meV and 105–120 meV. To analyse the vibrational states from graphene or residual contamination, the fitting windows were changed to 75–85 meV, 110–140 meV and 220–260 meV.

Although we tried to reduce the sample drift and charging issues, there are still some inevitable lattice distortions in most **q**-selective EELS mapping datasets, as shown in Extended Data Fig. 4. To correct such distortions, a standard affine transformation algorithm was used for each unit cell. The drift was compensated for by reconstructing the unit cell using the estimated affine transformation matrix obtained from the OpenCV package[46]. The random sample consensus method was implemented such that:

$$\begin{bmatrix} x \\ y \end{bmatrix} = \begin{bmatrix} a_{11} & a_{12} \\ a_{21} & a_{22} \end{bmatrix} \begin{bmatrix} X \\ Y \end{bmatrix} + \begin{bmatrix} b_1 \\ b_2 \end{bmatrix},$$

where x and y are the coordinates of the reference position (Sr or Ba atoms in our case), X and Y are the actual atom position, and the transformation matrix H is defined as $H = \begin{bmatrix} a_{11} & a_{12} & b_1 \\ a_{21} & a_{22} & b_2 \end{bmatrix}$. First, a 2D Gaussian fitting method in the Atomap software[44] was employed to identify the position of Sr or Ba atoms in both aHAADF-STEM images and the energy-filtered phonon map for 10–20 meV. These positions served as reference positions and measured positions, respectively. By combining a prediction based on the Ti atom positions in the 20–30 meV maps and manual selection, a series of discernible unit cells were marked with intact Sr or Ba atoms at the four corners of unit cells in the 10–20 meV maps and visible Ti atoms in the centre of the unit cells in the 20–30 meV and 30–40 meV maps. Then, a transformation matrix H was calculated by comparing the measured positions of four Sr or Ba atoms in each selected unit cell with their reference positions. All points inside that unit cell in the original image were mapped to their corresponding positions in the corrected images using the transformation matrix H obtained for that unit cell. The same H was also applied to correct all energy-filtered vibrational signal maps of the same unit cell. To address the sampling difference between the corrected and original images, bilinear interpolation was applied to individual vibrational signal maps. This interpolation method estimated the pixel values at non-integer positions by considering the intensities of neighbouring pixels to ensure a smooth and accurate representation of the original image during the transformation process. The resulting unit cells were then remapped back to their original undistorted cubic shape, as shown in Extended Data Fig. 5b,c.

Possible sources of map differences

There are a few discrepancies between the experimental signal maps and the simulated ones, mainly due to the residual sample drift, signal noise and spectral broadening. (1) In the 100–110 meV map of STO for an X' shift (Fig. 2e), the elongation observed at O3 columns was probably due to signal noise in this low-intensity range and to a residual sample drift. (2) Both the Ba and the Ti/O1 columns are visible in the 20–30 meV maps of BTO in Fig. 3e,i, but the corresponding simulation results contain only bright Ti/O1 columns. The percentage of Ba in 20–30 meV is 8.03% in the raw PhDOS of BTO. Thus, it is more probable that we can detect the vibrational states of Ba in this energy range. Besides, the average energy resolution of BTO datasets (12.9 ± 0.5 meV) was greater than that of STO (11.1 ± 0.7 meV), as shown in Extended Data Fig. 5d–g. Owing to the inadequate energy resolution, the vibrational states of Ba are broadened and spread into the energy range 20–30 meV. This is validated by the persistent presence of Ba columns in the signal maps for 20–22 meV, 22–24 meV and 24–26 meV in Extended Data Fig. 7g,h. Therefore, the detection of Ba is probably due to its non-zero atom-projected PhDOS and spectral broadening. (3) The observed shifts of Ti in the 20–30 meV and 50–60 meV maps for BTO in Fig. 3e,i may come from the residual sample drift, signal noise and spectral broadening. The inadequate energy resolution of the BTO datasets may lead to the involvement of Ba at 20–30 meV and subsequently deviate the position of the Ti signals. Owing to the limited spatial resolution of 1.5–2 Å, the atom positions in the vibrational signal maps are not accurate enough to directly measure the weak atomic displacement of Ti in the ferroelectric BTO. According to the scattering probability, the detected vibrational signal intensity is more representative of vibrational states of the probed atomic column and local symmetry of the **q**-selective EELS collection conditions. Thus, the observed shift of Ti should not be attributed to atomic displacement and is caused by experimental errors. (4) The ellipsoid-like features in the simulated maps in the high energy ranges (99.3 meV or 24 THz) in Fig. 3f,j were not observed in the corresponding experimental maps in Fig. 3e,i. The possible reasons are residual sample drift and signal noise in this low-intensity, high-energy range. However, this discrepancy did not influence the analysis of intensity contrasts between the O3 and the O2 columns.

First-principles calculations

The phonon dispersion and density of states simulations of STO and BTO at 0 K were first calculated using the Vienna Ab Initio Simulation Package at the level of the spin-polarized generalized-gradient approximation with the functional developed by Perdew–Burke–Ernzerhof[47]. The projector augmented wave method was adopted for the interaction between valence electrons and ionic cores[48,49]. In all density functional theory calculations, the energy cutoff for the plane wave basis expansion was set to 700 eV and the criterion for total energy convergence was set to 10^{-6} eV. A 4 × 4 × 4 supercell (320 atoms per supercell) was used to mimic STO or BTO, and all atoms were fully relaxed using the conjugated gradient method for energy minimization until the force on each atom became smaller than 0.01 eV Å^{-1}. The phonon dispersion and density of states were obtained using density functional perturbation theory[50].

Phonon dispersion calculations and molecular dynamics simulations

Molecular dynamics simulations were carried out using LAMMPS with DeePMD potentials trained for cubic STO and tetragonal BTO, respectively[31,51]. For STO, the potential successfully describes a structural phase transition from the low-temperature tetragonal phase to the high-temperature cubic phase in our previous work[31]. The phonon dispersion and PhDOS of the DeePMD potential at 0 K and 300 K in Extended Data Fig. 3a–f were calculated with the static displacement method using the phonoLAMMPS, DynaPhoPy and Phonopy packages[52–55]. The supercell was thereby set to 2 × 2 × 2 unit cells. The k-mesh for the integration of the PhDOS was set to 77 × 77 × 77. The microscopic anharmonic properties of the crystal were taken into account using the software DynaPhoPy integrated into the phonoLAMMPS interface. To accurately predict the LO–TO splitting at the Γ point, a non-analytic correction was applied to the final phonon dispersion and PhDOS calculations. The interpolation scheme in the Phonopy package used the dielectric constant and Born effective charges obtained from the density functional theory calculation. This comprehensive approach ensured that the phonon dispersion curve and density of states were calculated precisely by incorporating both the anharmonic properties and non-analytic corrections.

To simulate **q**-selective EELS, a series of molecular dynamics simulations were performed at 300 K when the STO was in its cubic phase. The supercell for the molecular dynamics calculations consisted of 12 × 12 × 60 unit cells. The supercell dimensions of 46.906 × 46.906 × 234.528 Å^3 were computed from the time average of the fluctuating supercell dimensions in a constant-temperature and constant-pressure molecular dynamics simulation (NPT ensemble) at a temperature of 300 K and a pressure of 0.0 bar. A time step of 1 fs was used in all molecular dynamics runs. After the box size had been fixed, a Langevin thermostat with a damping parameter of 100 fs was used to equilibrate the temperature to 300 K in a constant-temperature and constant-volume molecular dynamics simulation (NVT ensemble). This simulation was carried out to sample a set of 100 representative states of the vibrating atomic system, consisting of atomic positions and atomic velocities. These representative states of the system were extracted every 2,000 time steps (2 ps) after an initial equilibration of 5,000 time steps (5 ps), which guaranteed that they were uncorrelated.

The 100 representative states of the atomic system in the NVT ensemble served as initial inputs when computing 100 trajectories in a constant-energy molecular dynamics simulation (micro-canonical NVE ensemble). To form each NVE trajectory, we ran the simulation for 5,000 time steps (5 ps) and sampled the positions of all atoms every 10 time steps (10 fs) to obtain 5,000 position samples for each atom. We split each of the NVE trajectories into two parts with 2,500 position samples each, and the resulting 200 trajectories were used to simulate **q**-selective EELS, as described in 'FRFPMS simulations'.

A similar procedure was implemented for BTO. We trained a DeePMD potential for tetragonal BTO with a training dataset generated from DP-GEN (ref. 56) through a concurrent learning procedure consisting of training, exploration and labelling stages in each iteration. The training dataset is composed of over 12,000 frames of first-principles calculations with the PBEsol exchange correlation potential under various temperature ranges (50–400 K) and pressure conditions (1–1,000 kbar). The deep learning potential also successfully reproduces the consecutive phase transitions of BTO from cubic to tetragonal, orthorhombic and rhombohedral as the temperature is decreased. The phonon dispersion at 300 K in Extended Data Fig. 3g,h was obtained using the software DynaPhoPy. For the **q**-selective EELS simulations, 200 NVE trajectories of 2,500 position samples were generated using the same strategy used for STO. The supercell was set to 10 × 10 × 50 unit cells, resulting in total dimensions of $40.622 \times 39.980 \times 199.90$ Å^3. The only differences compared with the procedure for STO are that BTO is in its ferroelectric tetragonal phase at 300 K and that the anharmonicity of the potential energy surface causes a temperature-dependent shift in the equilibrium positions of Ti and O atoms relative to the positions of Ba atoms along the [001] axis. Therefore, the equilibrium positions of Ti and O atoms were determined from their time-averaged positions during long molecular dynamics trajectories at 300 K.

FRFPMS simulations

The electron scattering simulations (Figs. 2 and 3 and Extended Data Fig. 6e–h) were performed using the FRFPMS method, in which the inelastic signal was computed as the difference between the incoherent and the coherent averages of beam exit wavefunctions computed over structure snapshots, in which only displacements due to vibrational modes within a narrow range of frequencies were present[16,35,36]. The coherent term, identical to the elastic scattering signals, was excluded from the final simulated vibrational signal maps.

To extract structure snapshots representing certain phonon excitations for the cubic phase of STO, we implemented band-pass filtering on the 200 NVE trajectories consisting of 2,500 position samples. That is, for a selected NVE trajectory, we obtained the Fourier components of the (time-dependent) position samples of all atoms using a discrete Fourier transform, then we set all Fourier components to zero except for those inside a desired, narrow range of frequencies and finally performed an inverse Fourier transform to bring the band-pass-filtered atomic position samples back into the time domain. In this work, we considered frequency bands centred at frequencies from 1 THz to 25 THz in steps of 1 THz. Each band covered a frequency range of ±0.5 THz around said centre frequency. This was sufficient to encompass the whole range of vibrational frequencies (larger than 0.5 THz) where the PhDOS of STO is non-zero. From each of the 200 band-pass-filtered trajectories, we extracted one structure snapshot for each of the 25 frequencies.

These structure snapshots were used in the FRFPMS method to calculate the elastically and inelastically scattered electron intensities in each frequency bin and to determine the thermal ellipsoids shown in Fig. 5a,b, and Extended Data Fig. 9. All multislice calculations required for the FRFPMS method were carried out using the DrProbe software package[57]. The settings for the accelerating voltage, convergence semi-angle, EEA size and defocus in the multislice calculations closely followed the experimental conditions. The lateral grid size for the calculations was 576 × 576 and the supercell was divided into 600 approximately 0.4-Å-thick slices. We assumed for the multislice runs an isotropic Debye–Waller factor and absorptive potential, both parameterized by B_{iso} values (isotropic displacement parameters) of 0.5448 Å^2, 0.2948 Å^2 and 0.6711 Å^2 for Sr, Ti and O atoms, respectively. These values were determined from the ADPs in the molecular dynamics trajectories.

The FRFPMS simulations of BTO were performed analogously to those of STO: 200 structure snapshots were sampled from the 200 NVE trajectories using the same band-pass-filtering approach for each frequency between 1 THz and 25 THz in steps of 1 THz. These snapshots were used to calculate the inelastic scattering probability within the FRFPMS method and the calculation of the ADPs visualized as ellipsoids in Fig. 5 and Extended Data Fig. 9. The only differences in the FRFPMS simulations, shown in Fig. 3 and Extended Data Fig. 6, with respect to those for STO are that the lateral grid size was set to 480 × 480 for the multislice calculations and the supercell was divided into 500 approximately 0.4-Å-thick slices. Furthermore, the isotropic Debye–Waller factor and absorptive potential were parameterized by B_{iso} values of 0.407 Å^2, 0.396 Å^2 and 0.465 Å^2 for Ba, Ti and O atoms, respectively, as obtained by the DeePMD simulations at 300 K described above.

Data availability

The datasets generated and analysed during the current study are available from the corresponding authors upon request.

Code availability

The MATLAB code for the EELS data processing can be found on GitHub at https://github.com/PanGroup-UCI/Vibrational-EELS_background_subtraction.

43. Spiecker, E. Determination of crystal polarity from bend contours in transmission electron microscope images. *Ultramicroscopy* **92**, 111–132 (2002).
44. Nord, M., Vullum, P. E., MacLaren, I., Tybell, T. & Holmestad, R. Atomap: a new software tool for the automated analysis of atomic resolution images using two-dimensional Gaussian fitting. *Adv. Struct. Chem. Imaging* **3**, 9 (2017).
45. Yan, X. et al. Curvature-induced one-dimensional phonon polaritons at edges of folded boron nitride sheets. *Nano Lett.* **22**, 9319–9326 (2022).
46. Culjak, I., Abram, D., Pribanic, T., Dzapo, H. & Cifrek, M. A brief introduction to OpenCV. In *Proc. 35th International Convention MIPRO* (ed. Biljanović, P.) 1725–1730 (IEEE, 2012).
47. Perdew, J. P., Burke, K. & Ernzerhof, M. Generalized gradient approximation made simple. *Phys. Rev. Lett.* **77**, 3865–3868 (1996).
48. Blöchl, P. E. Projector augmented-wave method. *Phys. Rev. B* **50**, 17953–17979 (1994).
49. Kresse, G. & Joubert, D. From ultrasoft pseudopotentials to the projector augmented-wave method. *Phys. Rev. B* **59**, 1758–1775 (1999).
50. Gonze, X. & Lee, C. Dynamical matrices, Born effective charges, dielectric permittivity tensors, and interatomic force constants from density-functional perturbation theory. *Phys. Rev. B* **55**, 10355–10368 (1997).
51. Thompson, A. P. et al. LAMMPS – a flexible simulation tool for particle-based materials modeling at the atomic, meso, and continuum scales. *Comput. Phys. Commun.* **271**, 108171 (2022).
52. Carreras, A. phonoLAMMPS Documentation. *GitHub* https://github.com/abelcarreras/phonolammps (2023).
53. Carreras, A., Togo, A. & Tanaka, I. DynaPhoPy: a code for extracting phonon quasiparticles from molecular dynamics simulations. *Comput. Phys. Commun.* **221**, 221–234 (2017).
54. Togo, A., Chaput, L., Tadano, T. & Tanaka, I. Implementation strategies in phonopy and phono3py. *J. Phys. Condens. Matter* **35**, 353001 (2023).
55. Togo, A. First-principles phonon calculations with phonopy and phono3py. *J. Phys. Soc. Jpn* **92**, 012001 (2023).
56. Zhang, Y. et al. DP-GEN: a concurrent learning platform for the generation of reliable deep learning based potential energy models. *Comput. Phys. Commun.* **253**, 107206 (2020).
57. Barthel, J. Dr. Probe: a software for high-resolution STEM image simulation. *Ultramicroscopy* **193**, 1–11 (2018).
58. Momma, K. & Izumi, F. VESTA 3 for three-dimensional visualization of crystal, volumetric and morphology data. *J. Appl. Crystallogr.* **44**, 1272–1276 (2011).
59. Servoin, J. L., Luspin, Y. & Gervais, F. Infrared dispersion in $SrTiO_3$ at high temperature. *Phys. Rev. B* **22**, 5501–5506 (1980).
60. Stirling, W. G. Neutron inelastic scattering study of the lattice dynamics of strontium titanate: harmonic models. *J. Phys. C* **5**, 2711 (1972).
61. Zhou, J.-J., Hellman, O. & Bernardi, M. Electron-phonon scattering in the presence of soft modes and electron mobility in $SrTiO_3$ perovskite from first principles. *Phys. Rev. Lett.* **121**, 226603 (2018).
62. Scalabrin, A., Chaves, A. S., Shim, D. S. & Porto, S. P. S. Temperature dependence of the A_1 and E optical phonons in $BaTiO_3$. *Phys. Status Solidi B* **79**, 731–742 (1977).

63. Hermet, P., Veithen, M. & Ghosez, P. Raman scattering intensities in $BaTiO_3$ and $PbTiO_3$ prototypical ferroelectrics from density functional theory. *J. Phys. Condens. Matter* **21**, 215901 (2009).
64. Evarestov, R. A. & Bandura, A. V. First-principles calculations on the four phases of $BaTiO_3$. *J. Comput. Chem.* **33**, 1123–1130 (2012).
65. Ehsan, S., Arrigoni, M., Madsen, G. K. H., Blaha, P. & Tröster, A. First-principles self-consistent phonon approach to the study of the vibrational properties and structural phase transition of $BaTiO_3$. *Phys. Rev. B* **103**, 094108 (2021).

Acknowledgements The experimental work was primarily supported by the Department of Energy, Office of Basic Energy Sciences, Division of Materials Sciences and Engineering (Grant No. DE-SC0014430). Further support was provided by the National Science Foundation through a Materials Research Science and Engineering Center programme (Grant Award No. DMR-2011967). We acknowledge the use of facilities and instrumentation at the University of California (UC), Irvine's Materials Research Institute (IMRI). J.R. and P.M.Z. acknowledge the Swedish Research Council (Grant No. 2021-03848), Olle Engkvist's foundation (Grant No. 214-0331), Carl Trygger's Foundation, the Knut and Alice Wallenberg Foundation (Grant No. 2022.0079), and STINT's Joint Sweden–China Mobility programme (Grant No. CH2019-8211) for financial support. Simulations were enabled by resources provided by the National Academic Infrastructure for Supercomputing in Sweden and the Swedish National Infrastructure for Computing at the NSC Centre, which was partially funded by the Swedish Research Council (Grant Agreement Nos. 2022-06725 and 2018-05973). This work used the infrastructure for high-performance and high-throughput computing, research data storage and analysis, and scientific software tool integration built, operated and updated by the Research Cyberinfrastructure Center at UC, Irvine. The Research Cyberinfrastructure Center provides cluster-based systems, application software and scalable storage to directly support the UC, Irvine research community. We thank M. Xu and S. J. Kim (UC, Irvine) for the wet transfer of free-standing films, T. C. Lovejoy and N. Dellby (Bruker AXS LLC) for microscope alignment and high-order EELS aberration correction, and B. Liao (UC, Santa Barbara) for valuable discussions.

Author contributions X.P. conceived this project and designed the studies, with contributions from J.R., R.W. and X.Y. X.Y. and Y.H. performed the STEM-EELS experiments and analysed all datasets with the help of H.Y., C.A.G. and T.A. Y.H. performed the drift correction. P.M.Z. and J.R. designed and performed the molecular dynamic-based calculation of vibrational spectra with the help of Y.H., R.H. and Z.Z. J.L. and R.W. conducted the first-principles calculations. The free-standing STO and BTO films were synthesized and provided by H.S. and Y.N. All authors discussed and commented on the results. The paper was prepared by X.Y., P.M.Z., J.R., R.W. and X.P. with contributions from all other co-authors.

Competing interests The authors declare no competing interests.

Additional information

Correspondence and requests for materials should be addressed to Ruqian Wu, Ján Rusz or Xiaoqing Pan.

Peer review information *Nature* thanks Claudio Cazorla, Sang Ho Oh and the other, anonymous, reviewer(s) for their contribution to the peer review of this work.

Reprints and permissions information is available at http://www.nature.com/reprints.

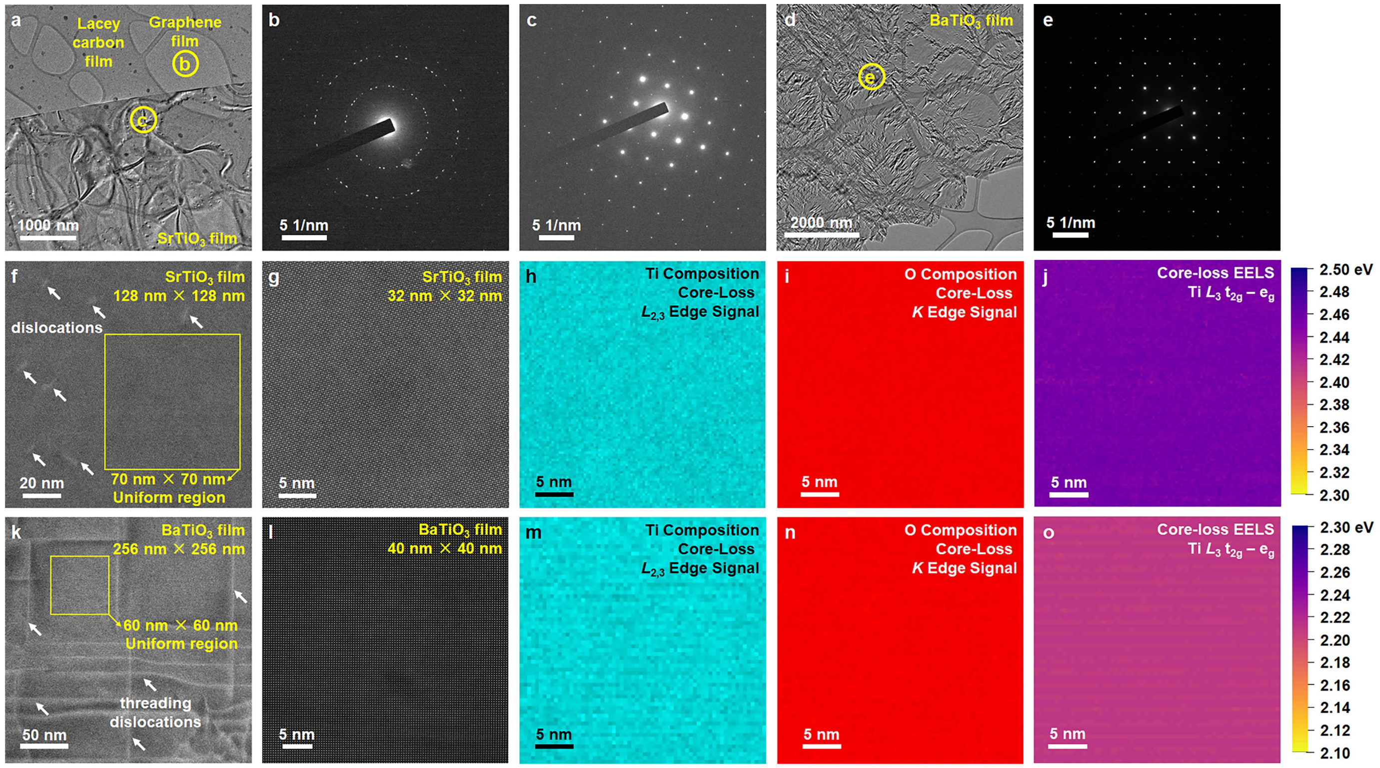

Extended Data Fig. 1 | TEM analysis of STO and BTO films supported by a few-layer graphene suspended on a lacey carbon film. a, A low-magnification TEM image of the STO film supported by a graphene film with 3–6 layers on a lacey carbon TEM grid. All experiments were conducted on the suspended perovskite/graphene regions without the carbon film. **b**,**c**, Selected area diffraction patterns of a pure graphene region (**b**) and a STO/graphene region (**c**) as marked in (**a**), respectively. There are six sets of typical diffraction patterns of graphene in (**b**), indicating the layer number is probably six with random stacking orders. The diffraction pattern of STO along [001] direction is clearly visible in (**c**), while the diffraction patterns of graphene are hardly visible due to its thin thickness. **d**, A low-magnification TEM image of the BTO film supported by a graphene film on a lacey carbon TEM grid. **e**, Selected area diffraction pattern of a BTO/graphene region as marked in (**d**). **f**,**g**, Low- (**f**) and medium-magnification (**g**) STEM images of the STO film. **h**-**j**, Core-loss EELS analysis of elemental distribution and chemical composition of the STO film using Ti $L_{2,3}$ edge signal (**h**), O K edge signal (**i**), and energy difference between t_{2g} and e_g peaks in the Ti L_3 edge (**j**). **k**,**l**, Low- (**k**) and medium-magnification (**l**) STEM images of the BTO film. **m**-**o**, Core-loss EELS analysis of elemental distribution and chemical composition of the BTO film using Ti $L_{2,3}$ edge signal (**m**), O K edge signal (**n**), and energy difference between t_{2g} and e_g peaks in the Ti L_3 edge (**o**). Although there are dislocations in both STO and BTO as the white segments and lines marked in (**f**) and (**k**), we can easily find defect-free regions larger than 50 nm × 50 nm in both samples. All vibrational EELS hyperspectral imaging datasets were acquired from those single-crystalline regions without any visible contamination and away from dislocations and other defects as shown in (**g**) and (**l**). All investigated regions were also tilted on zone-axis as shown in (**c**) and (**e**). Thus, the collected phonon signals cannot be interfered with by defects, contamination, overall strain field or bent contours. The elemental distributions of Ti and O based on core-loss EELS signals are uniform in both samples. The splitting of t_{2g} and e_g peaks as the energy difference between these two peaks in the Ti L_3 edge, which is widely used to estimate the change of valence state of Ti, is 2.44–2.46 eV in STO (**j**) and 2.20–2.21 eV in BTO (**o**), respectively. Since the oxygen vacancy and associated valence state change of Ti can lead to a reduction of the splitting for about 0.5 eV in the literature[17], core-loss EELS results can exclude the occurrence of oxygen vacancies or other compositional variations in the investigated regions. Therefore, STEM images and elemental mapping results can rule out the interference from dislocations, oxygen vacancies, and composition changes in the studied areas for the phonon anisotropy results.

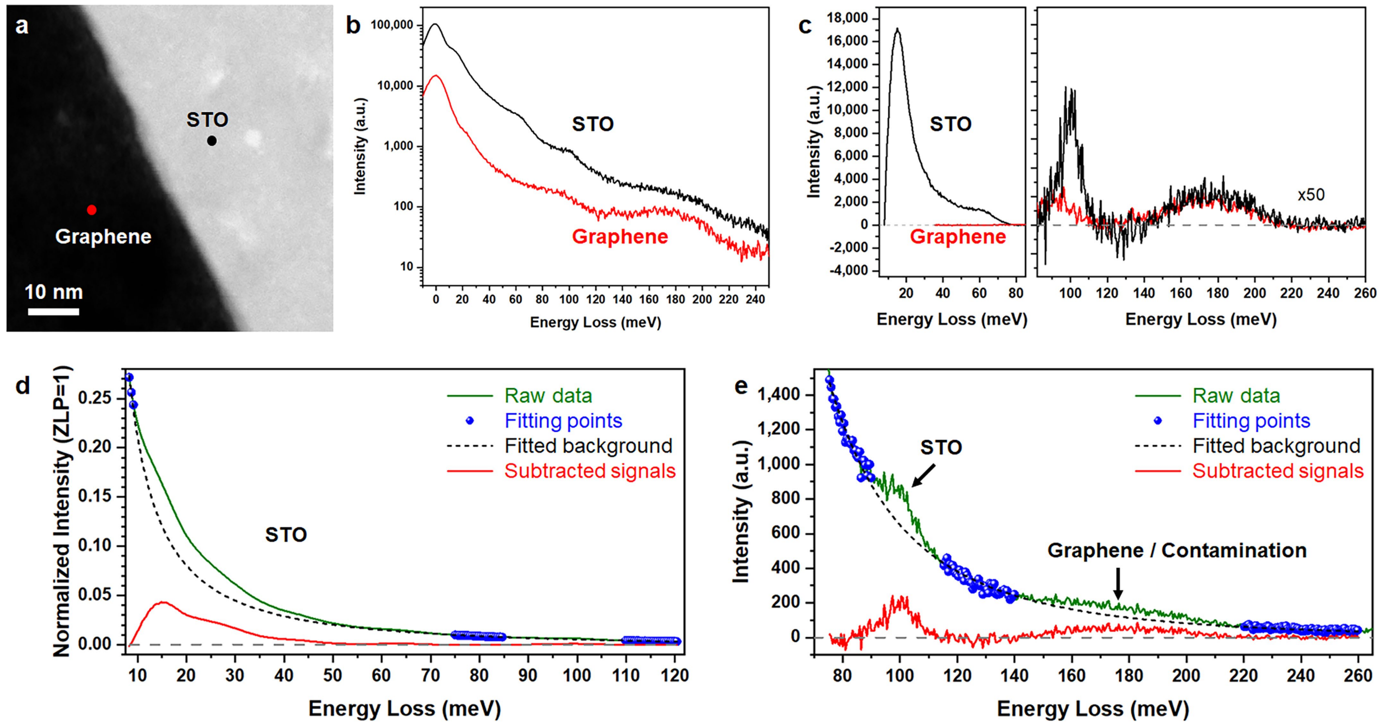

Extended Data Fig. 2 | Background subtraction and comparison of vibrational signals between STO and graphene films. **a**, A HAADF STEM image at the edge of STO film. The dark region is graphene, while the bright region is STO supported by graphene. **b**, Raw dark-field vibrational spectra at STO and graphene regions as marked by black and red dots in (**a**). Both spectra were obtained by summing 200 frames of 1 s exposure spectra. The spectrum collected at the graphene region contains two broad peaks at 60–100 and 140–200 meV, in agreement with previous studies[11,12]. **c**, Background-subtracted spectra at STO and graphene regions. In the energy range of 10–80 meV energy range, the vibrational signals of graphene are negligible compared to those of STO. In the energy range of 80–120 meV, the intensity of vibrational signals of STO is about six times that of graphene. The broad peak in 140–200 meV originates from phonon modes in graphene or other residual contamination. Therefore, we can ignore the bulk phonon modes of graphene and residual contamination in the energy range of interest for STO and BTO. **d**, Background-subtracted spectrum containing STO phonon structure in the energy range of 10–110 meV. The spectrum is used in Fig. 1b. **e**, Background-subtracted spectrum containing vibrational states of graphene and residual contamination in the energy range of 140–200 meV. The raw spectrum is duplicated from the black curve in (**b**). The blue dots are fitting windows, while the black dashed lines are the fitted backgrounds using a power law function.

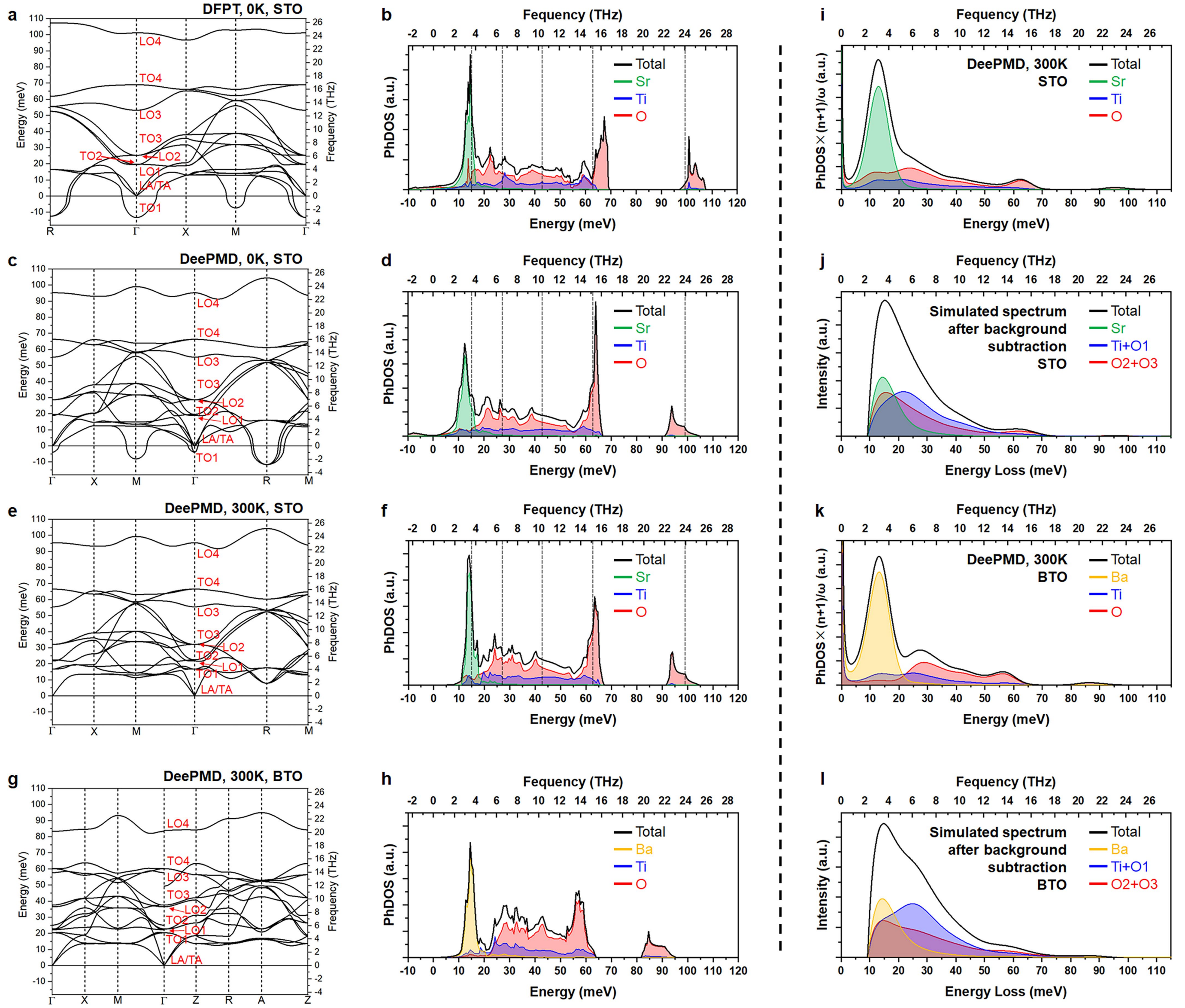

Extended Data Fig. 3 | Simulated phonon dispersion curves, PhDOS, and vibrational spectra of STO and BTO using different methods. a, Density functional perturbation theory (DFPT)-simulated phonon dispersion curves of STO at 0 K. **b**, PhDOS and atom projected PhDOS associated with (**a**). **c**, Phonon dispersion curves of STO simulated from the DeePMD potential at 0 K using the finite displacement method. **d**, PhDOS and atom projected PhDOS associated with (**c**). **e**, Phonon dispersion curves of STO simulated from the DeePMD potential at 300 K using the finite displacement method. **f**, PhDOS and atom projected PhDOS associated with (**e**). **g**, Phonon dispersion curves of BTO simulated from the DeePMD potential at 300 K using the finite displacement method. **h**, PhDOS and atom projected PhDOS associated with (**g**). **i**, Modified PhDOS of STO and atom projected PhDOS with a 7 meV Gaussian broadening after involving phonon occupation number and phonon energy. **j**, Simulated vibrational EEL spectrum of STO with a 13 meV Gaussian broadening after subtracting the background. **k**, Modified PhDOS of BTO and atom projected PhDOS with a 7 meV Gaussian broadening after involving phonon occupation number and phonon energy. **l**, Simulated vibrational EEL spectrum of BTO with a 13 meV Gaussian broadening after subtracting the background. In (**b, d, f, i, j**), green, blue, and red curves represent the projected PhDOS of Sr, Ti, and O atoms, respectively. In (**h, k, l**), orange, blue, and red curves represent the projected PhDOS of Ba, Ti, and O atoms, respectively. LA/TA modes and four pairs of LO/TO modes are labeled at the Γ point for each phonon dispersion curve. Only three pairs of LO/TO modes are infrared active, but all should be visible in vibrational EELS results due to their different selection rules and the use of a large convergence semi-angle in our experiments. Five vertical dashed lines indicate the experimental peak centers of P1–P5 in STO at 14.6 meV, 24.4 meV, 41.1 meV, 63.3 meV, and 98.7 meV, respectively. At 0 K, both DFPT- and DeePMD-based phonon dispersion curves show obvious imaginary modes at the R and M points due to the octahedral rotation instabilities and at the Γ point due to polar instability[37]. Consequently, non-zero signals are present in the negative energy ranges of corresponding PhDOS curves. At 300 K, the absence of imaginary modes indicates the dynamic stability of such a structure at room temperature. All three simulated PhDOS curves reasonably match experimental peak centers, despite some discrepancies in energy positions. Among them, DeePMD-simulated PhDOS at 300 K agrees best with experimental peak values, especially for P1–P4. The overall phonon band structure of BTO is similar to that of STO but with noticeable red-shifts in the high-energy O-related peaks (P4 and P5) and blue-shifts in the Ti-O related peaks (P2 and P3). To make a more coherent comparison, we multiplied the simulated PhDOS with $(n+1)/\omega$, where n is the phonon occupation number obeying the Boltzmann distribution and ω is the phonon energy, to convert to vibrational EELS signals. After the modification, the high-energy phonon modes above 30 meV (P3, P4, and P5) in (**i**) and (**k**) are significantly suppressed and look more consistent with those in experimental spectra. We also provide simulated vibrational spectra using our FRFPMS method in (**j**) and (**l**), showing even better consistency with experimental spectra in terms of the intensity ratio of P1 and P2 in the low energy ranges. The remaining differences are probably due to the finite size of simulation supercell and associated issues of LO/TO splitting in periodic supercells.

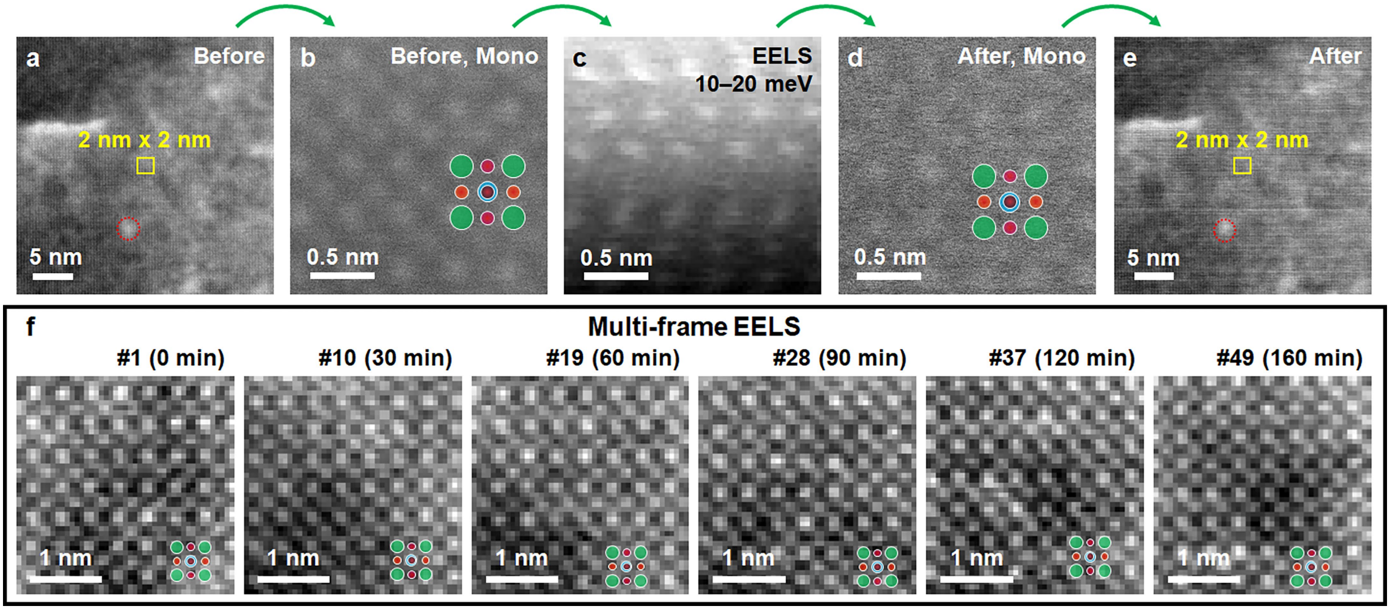

Extended Data Fig. 4 | Procedure of q-selective EELS data collection. a, Low magnification STEM image before EELS acquisition. The central region with a size of 2 nm × 2 nm (the yellow box) was used to acquire an atomic resolution **q**-selective EELS hyperspectral image dataset. **b**, High magnification STEM image acquired at the yellow box in (**a**) with monochromation before EELS acquisition. **c**, Hyperspectral image dataset with 60×60 pixel area. The displayed intensity is the integrated raw signal in the 10–20 meV range. The total acquisition time for this dataset is about 60 min. **d**, High magnification STEM image acquired at the yellow box in (**e**) with monochromation after EELS acquisition. **e**, Low magnification STEM image after EELS acquisition. The atomic structure of STO overlaps on the atomic resolution STEM images in (**b**) and (**d**). The region of interest is chosen with perfect STO crystalline structure in absence of any defects. The crystalline structure is still retained after the long EELS acquisition. No detectable contamination occurs during this experiment as shown in (**e**). The red dashed circle indicates a defective region to be used to measure the sample drift before and after the EELS acquisition. The sample drift was 0.20 nm in this case with a sample drift rate of about 0.2 nm/h. **f**, Sequential STEM images captured during multi-frame EELS acquisition on STO of 3 nm × 3 nm. The frame number and time are labeled on top of each image with an acquisition time of 200 s per frame. A single-unit-cell atomic structure of STO is overlapped on atomic resolution STEM images, and the green, cyan, black, purple, and orange dots denote Sr, Ti, O1, O2 (apical oxygen), and O3 (equatorial oxygen), respectively.

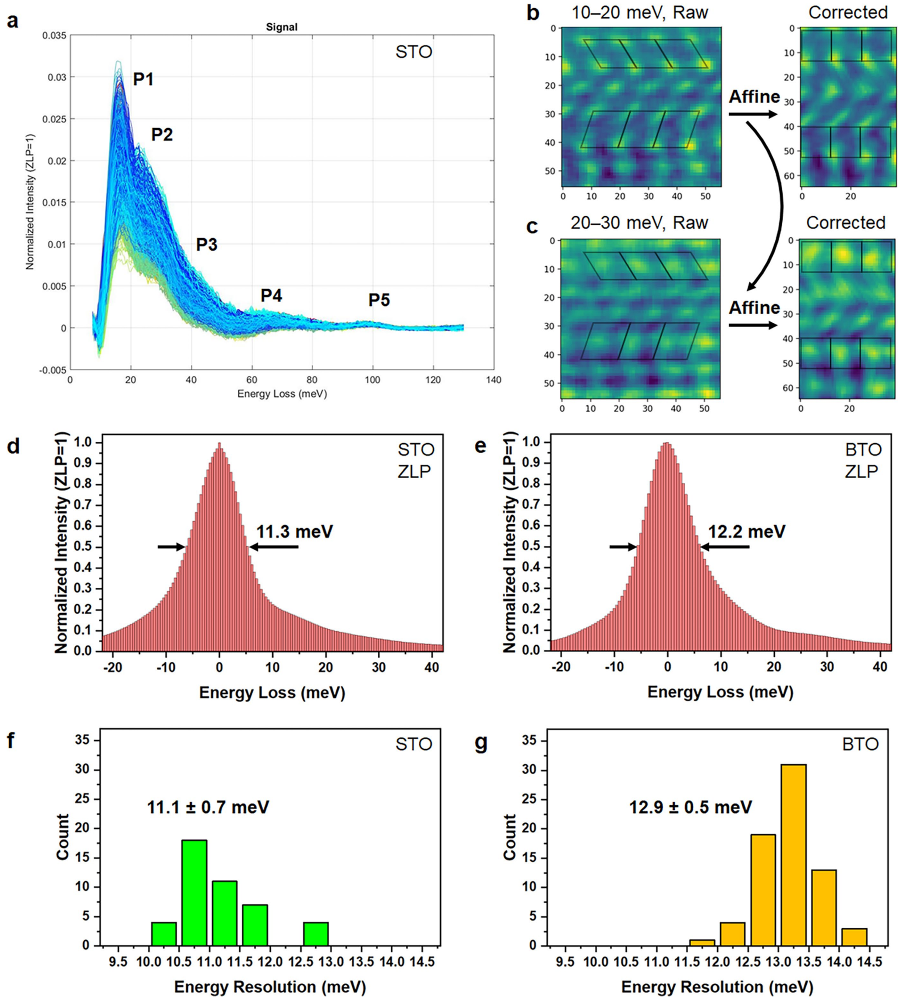

Extended Data Fig. 5 | Data analysis, drift correction, and the influence of energy resolution. **a**, Background subtracted vibrational spectra in one hyperspectral image dataset. **b**, Affine transformation of the raw map in 10–20 meV to reconstruct the square lattice of STO by first finding the center of bright spots at Sr positions and applying a series of affine transformations for each unit cell. **c**, Affine transformation of the raw map in the 10–20 meV energy range to reconstruct the square lattice of STO by using the same transformation matrix *H* measured in individual unit cells in (**b**). The selected unit cells are indicated as parallelograms and then reconstructed to squares in (**b**) and (**c**). **d,e**, Representative vibrational spectra of STO (**d**) and BTO (**e**) containing ZLPs with a full-width at half-maximum of 11.3 meV and 12.2 meV, respectively. **f,g**, Distribution of energy resolution of all datasets on STO (**f**) and BTO (**g**). We made statistical analysis of all experimental datasets of both STO and BTO and found that the average energy resolution of STO datasets (11.1 ± 0.7 meV) was smaller than that of BTO (12.9 ± 0.5 meV).

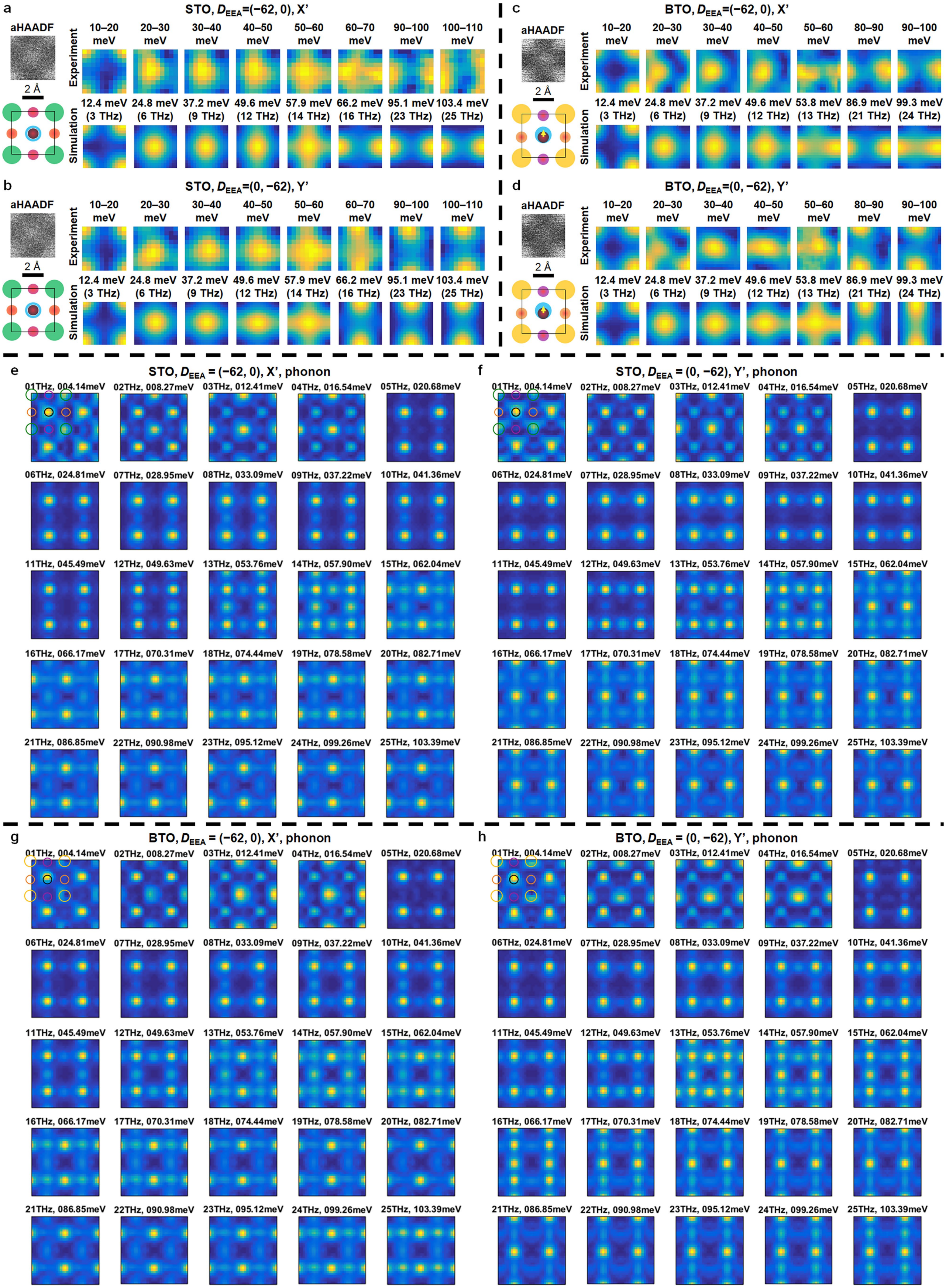

Extended Data Fig. 6 | See next page for caption.

Extended Data Fig. 6 | Atomic resolution vibrational signal maps with single unit cell regions and raw simulation results. a,b, Experimental vibrational signal maps of STO in different energy ranges with $\boldsymbol{D}_{\mathrm{EEA}} = (-62, 0)$ or an X' shift (**a**), and with $\boldsymbol{D}_{\mathrm{EEA}} = (0, -62)$ or a Y' shift (**b**) along with aHAADF images and atomic structures, obtained from the same datasets in Fig. 2. **c,d**, Experimental vibrational signal maps of BTO in different energy ranges with $\boldsymbol{D}_{\mathrm{EEA}} = (-62, 0)$ or an X' shift (**a**), and with $\boldsymbol{D}_{\mathrm{EEA}} = (0, -62)$ or a Y' shift (**b**) along with aHAADF images and atomic structures, obtained from the same datasets in Fig. 2. The green, gold, cyan, black, purple, and orange dots denote Sr, Ba, Ti, O1, O2 (apical oxygen), and O3 (equatorial oxygen), respectively. Scale bars are 2 Å. **e**–**h**, Raw simulated energy-filtered vibrational signal maps from 1 THz and 25 THz of STO for the X' shift (**e**), STO for the Y' shift (**f**), BTO for the X' shift (**g**), and BTO for the Y' shift (**h**). The size of each image is 8 Å × 8 Å. The energy bin width is 1 THz, and the labeled energy is the bin center. The atomic structure overlaps on the first signal map of each situation as A-site (Sr or Ba) atoms residing at the top-left corner of each image.

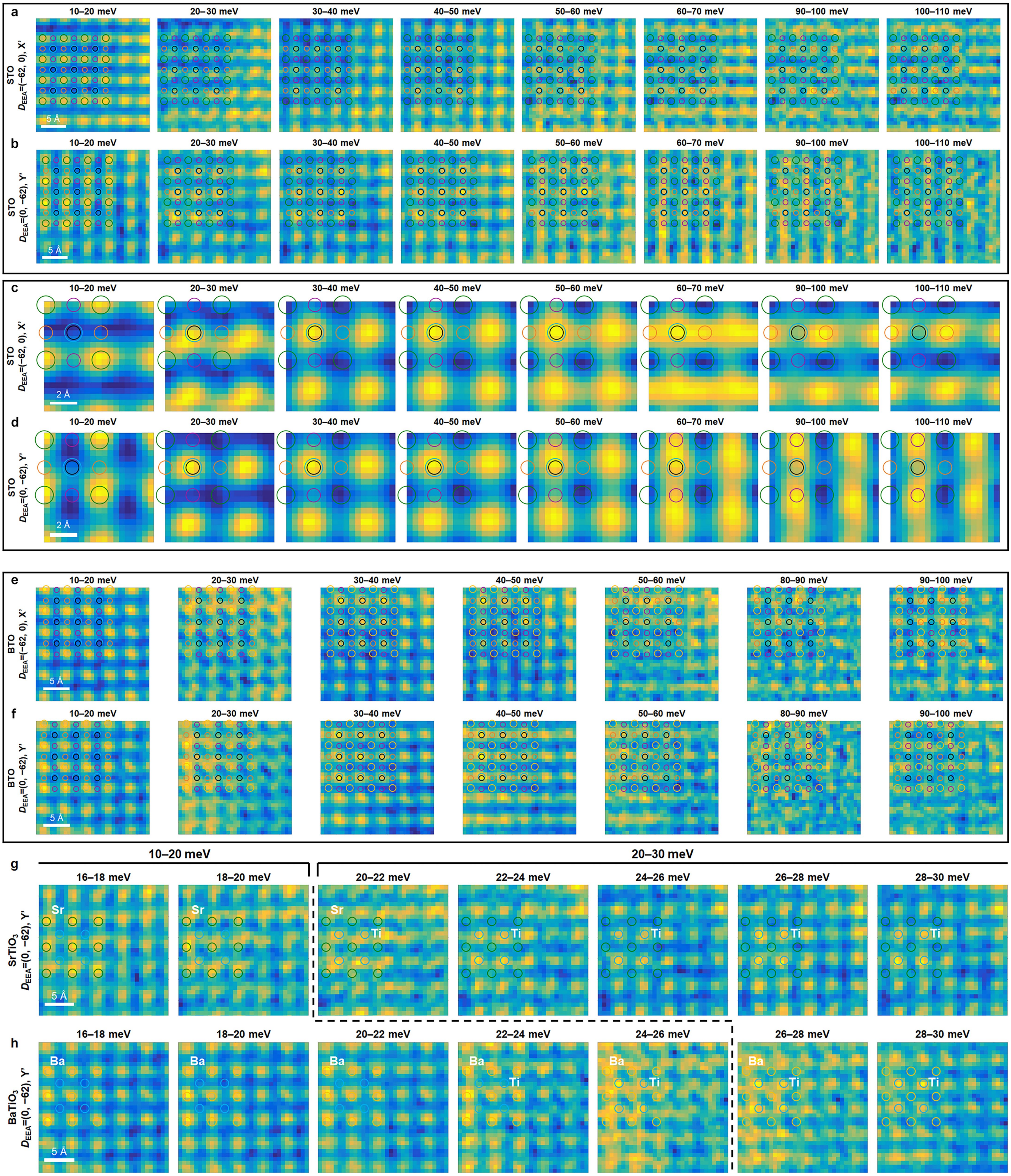

Extended Data Fig. 7 | See next page for caption.

Extended Data Fig. 7 | More atomic resolution vibrational signal mapping of STO and BTO over larger regions. a,b, Experimental vibrational signal maps of STO on a 2.3 nm × 2.3 nm region in different energy ranges with $\boldsymbol{D}_{\mathrm{EEA}} = (-62, 0)$ or an X' shift (**a**), and with $\boldsymbol{D}_{\mathrm{EEA}} = (0, -62)$ or a Y' shift (**b**). **c**, Vibrational signal maps averaged from 20 unit cells in (**a**). **d**, Vibrational signal maps averaged from 16 unit cells in (**b**). Displayed maps in (**c**) and (**d**) are duplicated from averaged single-unit-cell results to 2×2 unit cells for visual clarity. **e,f**, Experimental vibrational signal maps of BTO on a 2.3 nm × 2.3 nm region in different energy ranges with $\boldsymbol{D}_{\mathrm{EEA}} = (-62, 0)$ or an X' shift (**e**), and with $\boldsymbol{D}_{\mathrm{EEA}} = (0, -62)$ or a Y' shift (**f**). An atomic structure of STO or BTO is overlapped on all vibrational signal maps, and the green, gold, cyan, black, purple, and orange circles denote Sr, Ba, Ti, O1, O2 (apical oxygen), and O3 (equatorial oxygen), respectively. **g,h**, Vibrational signal maps of STO **(e)** and BTO **(f)** with a smaller energy bin size of 2 meV. The dashed lines indicate the boundary between A-site dominant signal maps and Ti dominant ones. In (**h**), Ba columns are still observable in the signal maps of 20–22 meV, 22–24, and 24–26 meV, while Ti/O1 columns exhibit the prominent intensity only when the energy range is above 24–26 meV. By contrast, the vibrational intensity of Sr columns in STO becomes very weak when the energy range is above 18–20 meV, in parallel with increasingly visible Ti/O1 columns in (**g**). Therefore, we indeed detected noticeable vibrational intensity at Ba columns in 20–30 meV due to its non-zero atom-projected PhDOS and spectral broadening.

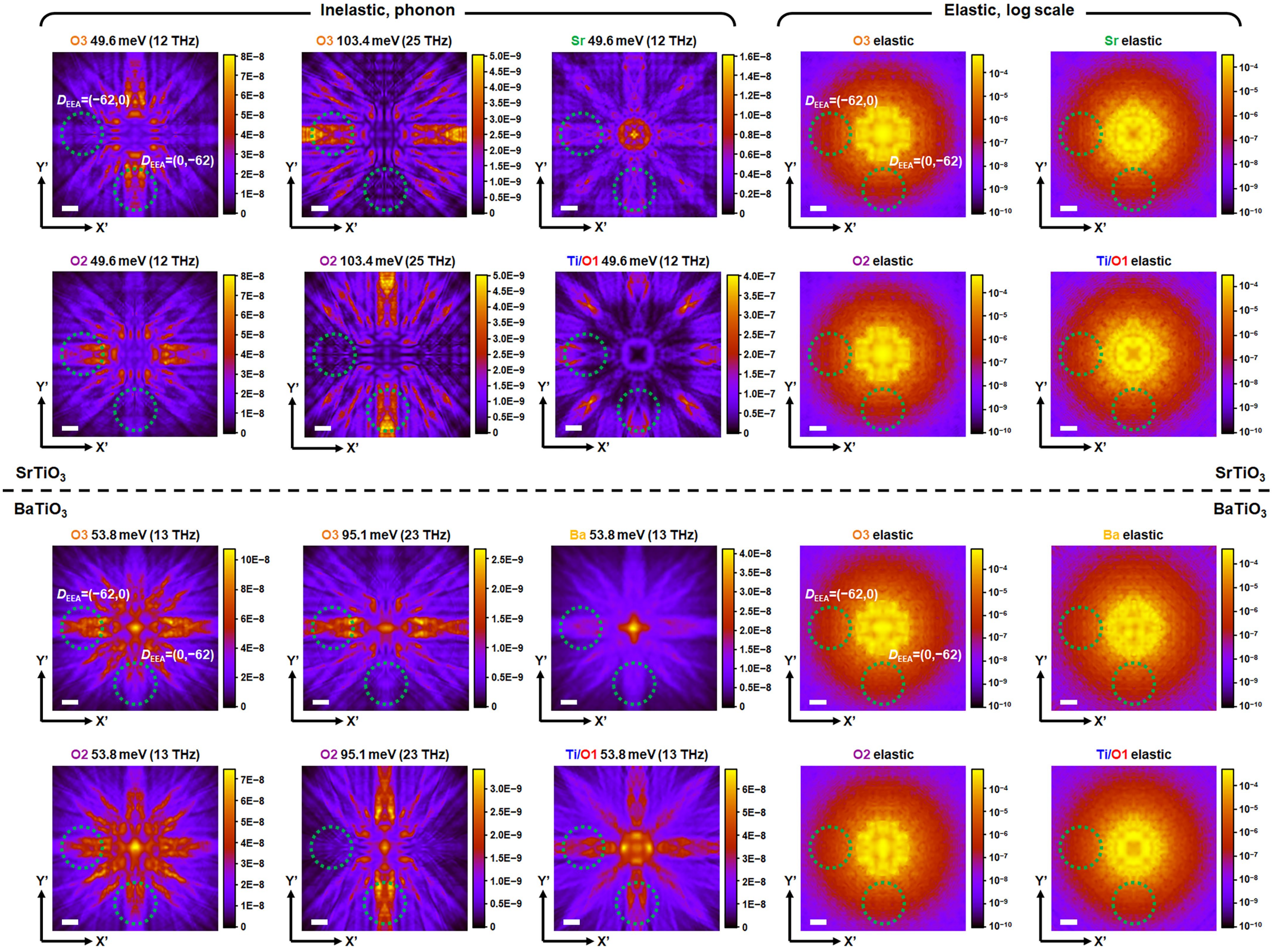

Extended Data Fig. 8 | Simulated position-dependent energy-filtered diffraction patterns of both inelastically and elastically scattered electrons of STO along [001] (upper) and BTO along [010] (lower) at selected energies. 49.6 meV (12 THz) and 103.4 meV (25 THz) are selected for STO, while 53.8 meV (13 THz) and 95.1 meV (23 THz) are selected for BTO. The energy bin width is 1 THz. The atomic positions (= O3, O2, Sr or Ba, and Ti/O1) being placed by the electron beam and the energy values are labeled at the top of diffraction patterns. All inelastic signals with certain phonon energy losses (left three columns) are on a linear scale, whereas all elastic signals (right two columns) are on a logarithmic scale. Two dashed green circles indicate EEA positions of $\boldsymbol{D}_{\mathbf{EEA}}$ = (−62, 0) and $\boldsymbol{D}_{\mathbf{EEA}}$ = (0, −62), respectively. Scale bars are all 20 mrad.

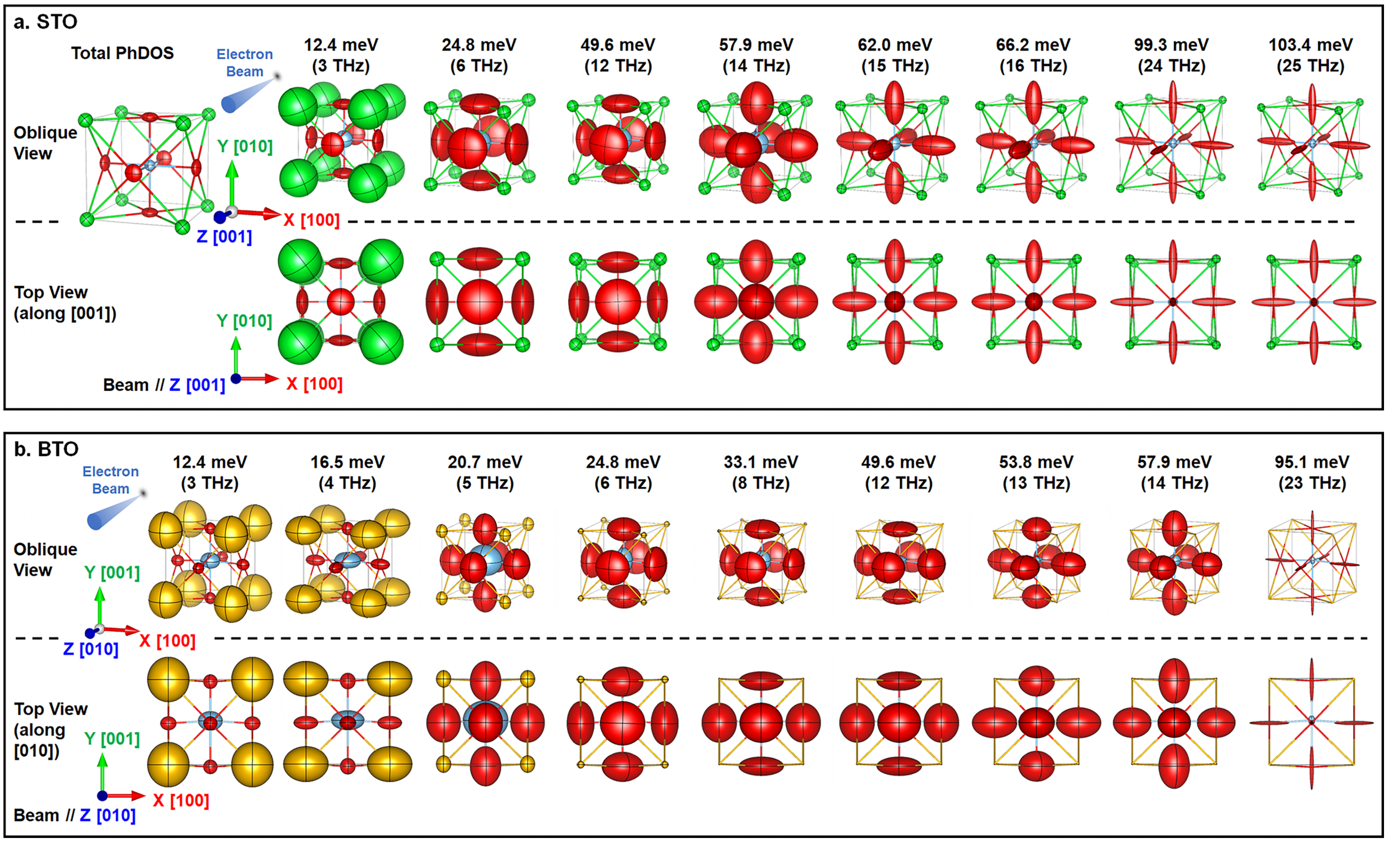

Extended Data Fig. 9 | Three-dimensional maps of simulated ADPs of all atoms in STO and BTO at selected energies. **(a)** Maps of ADPs for STO in oblique views (upper) and top views along [001] (lower). The thermal ellipsoids for the total PhDOS (the left most image) are drawn such that each atom is found with a probability of 99% within the volume of the ellipsoid using the VESTA software[58]. The shape of thermal ellipsoids represents the isotropy or anisotropy of atomic displacements. In all other images to the right, the frequency-dependent ADPs of all atoms are rescaled to highlight the relative sizes of displacements at the corresponding energy. The rescaling factors for these images are approximately 264 (3 THz), 943 (6 THz), 5642 (12 THz), 5087 (14 THz), 2394 (15 THz), 5495 (16 THz), 15505 (24 THz), and 41480 (25 THz). The electron beam in STO experiments was parallel to the Z axis or [001] direction. In the map of total PhDOS to the left, the thermal vibrations of Sr and Ti atoms are isotropic, but oxygen atoms exhibit an anisotropy consistent with ref. 5. The energy-dependent displacement ellipsoids, shown to the right, extend this consideration: Sr and Ti atoms exhibit isotropic displacements at all energies, indicating the homogeneity of corresponding phonon eigenvectors, and the anisotropy of oxygen vibrations evolves as a function of frequency. Oxygen displacements form an oblate ellipsoid ($U_{11}/U_{22} < 1$) lying on {100} planes in the lower energy range. The ellipsoids associated with oxygen atoms transform to prolate ellipsoids ($U_{11}/U_{22} > 1$) elongated along <100> directions at higher energies. **(b)** Maps of ADPs for BTO in oblique views (upper) and top views along [010] (lower). In all other images to the right, the frequency-dependent ADPs of all atoms are rescaled to highlight the relative sizes of displacements at the corresponding energy. The rescaling factors for these images are approximately 31 (3 THz), 122 (4 THz), 187 (5 THz), 70 (6 THz), 130 (8 THz), 316 (12 THz), 292 (13 THz), 350 (14 THz), and 5912 (23 THz). The electron beam in BTO experiments was parallel to the Z axis or [010] direction. Note that the thermal ellipsoids of both Ba and Ti are no longer isotropic in BTO.

Extended Data Table 1 | Comparison of experimental and calculated phonon energies of STO and BTO from the literature and our work

Methods and Source	Phonon Energy at the Γ point (meV)							
	TO1	**LO1**	**TO2**	**LO2**	**TO3**	**LO3**	**TO4**	**LO4**
			Cubic $SrTiO_3$					
Optical conductivity, 300 K [32]	11.65	21.13	21.79	-	-	58.95	67.43	98.72
Infrared, 300 K [33]	11	22	22	-	-	57	68	101
Infrared, 300 K [59]	11.03	21.34	21.73	-	-	58.88	67.41	98.71
Inelastic neutron scattering, 297 K [60]	11.37	21.01	21.01	32.88	32.88	56.66	67.83	102.15
DFT[a], 0 K [33]	10.04	19.09	21.45	27.66	27.83	54.3	69.55	100.05
TDEP[b] DFT, 300 K [61]	12.62	20.79	22	29.85	29.85	55.98	67.06	96.42
This work, DeePMD, 300 K	16.74	21.78	22.58	32.17	32.17	55.56	66.65	95.49
			Tetragonal $BaTiO_3$					
Raman, 300 K [62]	22.07	23.43	34.22	-	-	58.39	63.84	89.89
Raman, 300 K [63]	19.96	22.32	37.44	-	-	56.04	62.86	87.41
DFT, 0K [64]	21.45	22.07	22.94	39.43	39.67	58.77	60.01	87.65
QHA-SCP[c] DFT, 400 K [65]	17.32	22.97	31.63	36.48	37.28	55.83	59.26	90.30
This work, DeePMD, 300 K	20.39	22.48	25.14	36.60	37.63	57.75	60.38	83.45

[a] DFT: Density functional theory.

[b] TDEP: Temperature-dependent effective potential

[c] QHA-SCP: Quasiharmonic approximation - self-consistent phonon

Our simulation results match well with the energy positions of most phonon modes in both STO and BTO, especially for the high energy phonon modes above 30 meV and show only blue shifts on low energy phonon modes (TO1 and LO1) of STO. References 59–65.